scientific reports

Check for updates

OPEN

Dual-fluorescent starch biopolymer films containing 5-(4-nitrophenyl)-1,3,4-thiadiazol-2-amine powder as a functional nanofiller

Anita Kwaśniewska[1], Katarzyna Orzechowska[2], Klaudia Rząd[3], Luca Ceresa[4], Małgorzata Figiel[5], Anna A. Hoser[6], Maurycy E. Nowak[6], Dariusz Karcz[7], Bożena Gładyszewska[3], Grzegorz Gładyszewski[1], Monika Srebro-Hooper[2]✉ & Arkadiusz Matwijczuk[3]✉

Physical and photophysical properties of starch-based biopolymer films containing 5-(4-nitrophenyl)-1,3,4-thiadiazol-2-amine (NTA) powder as a nanofiller were examined using atomic force microscopy (AFM), Fourier-transform infrared spectroscopy (FTIR), stationary UV-Vis and fluorescence spectroscopy as well as resonance light scattering (RLS) and time-resolved measurements, and where possible, analyzed with reference to pristine NTA solutions. AFM studies revealed that the addition of NTA into the starch biopolymer did not significantly affect surface roughness, with all examined films displaying similar Sq values ranging from 70.7 nm to 79.7 nm. Similarly, Young's modulus measurements showed no significant changes after incorporating the 1,3,4-thiadiazole. Adhesion force and water contact angle assessments demonstrated that the films maintained high hydrophilicity (water wetting) across all examined films. Color analysis corroborated the anticipated trend, showing that increasing additive content resulted in decreased lightness and increased yellowness. Interestingly, however, while in polar isopropanol solvent at low concentration, NTA shows a typical single-band emission, centered at 410 nm and a slight enhancement of the band on the long-wavelength side around 530 nm, its incorporation into the biopolymer matrices results in the appearance of dual fluorescence signal with maxima at 430 and 530 nm. Concentration-dependence emission experiments, demonstrating that with even a slight increase of the amount of NTA in solution, an additional, weak long-wavelength emission band emerged within the spectral range corresponding to the intensive band in the biopolymer film, along with results of the performed quantum-chemical studies, including both the monomeric and aggregated (dimer and trimer) models, conclusively unveil that the dual fluorescence observed in starch/NTA films is due to molecular aggregation effects resulting in aggregation-induced emission. This study underscores the potential of NTA as an additive in biobased polymer films, furnishing them with new photophysical features without substantially altering their surface properties and thus enabling their extended applications.

Over the recent years, due to both economic and environmental issues, the increasing interest in the development and engineering of natural-origin materials has been observed[1–3]. In particular, broad studies on biobased polymers have demonstrated their appealing properties and potential applications in various areas, and resulted in growing substitution of synthetic materials wherever biodegradability, biocompatibility and non-toxicity are especially valued[4]. These features, alongside with their sustainability and affordability, combined with the

[1]Department of Applied Physics, Faculty of Mechanical Engineering, Lublin University of Technology, Nadbystrzycka 38, Lublin 20-618, Poland. [2]Department of Theoretical Chemistry, Faculty of Chemistry, Jagiellonian University, Gronostajowa 2, Kraków 30-387, Poland. [3]Department of Biophysics, Faculty of Environmental Biology, University of Life Sciences in Lublin, Akademicka 13, Lublin 20-950, Poland. [4]Department of Physics and Astronomy, Texas Christian University, Fort Worth, TX 76109, USA. [5]Department of Physical Biochemistry, Faculty of Biochemistry, Biophysics and Biotechnology, Jagiellonian University, Gronostajowa 7, Kraków 30-387, Poland. [6]Faculty of Chemistry, University of Warsaw, Pasteura 1, Warszawa 02-093, Poland. [7]Faculty of Chemical Engineering and Technology, Department of Chemical Technology and Environmental Analytics (C1), Cracow University of Technology, Krakow 31-155, Poland. ✉email: monika.srebro@uj.edu.pl; arkadiusz.matwijczuk@up.lublin.pl

relative ease of tuning their properties via structure and composition modifications, make such biopolymers emerging materials in versatile applications. For example, starch, cellulose, chitin and other polysaccharides after reinforcement of the structure have been utilized as cost-effective materials for food-packaging[5,6]. Modified starch-lignin materials have been proposed as biodegradable matrices for fertilizers[7]. Finally, due to a wide array of their physicochemical properties starch-based polymers have been also thoroughly studied for biomedical purposes, for example as potential frameworks for tissue regeneration, materials for implants and time-controlled drug delivery systems[8,9]. An important strategy in engineering biopolymers towards functional materials is the use of nanofillers that commonly fulfil the reinforcing function by improving the mechanical, thermal, and barrier properties of biomaterials, but that could also – when appropriately chosen – furnish such materials with new features and extend their functionality[10,11]. One could mention for instance numerous literature reports presenting studies on developments of biodegradable food packaging showing antifungal properties by employing various types of nanofillers[12–14]. In the broad context of designing new biopolymeric materials, 1,3,4-thiadiazole derivatives appear as particularly promising functional nanofiller candidates since they exhibit a broad spectrum of interesting physicochemical properties and established applications in various areas of chemistry, including pharmaceutics, agriculture and materials science[15–17].

1,3,4-thiadiazoles include aromatic five-membered ring comprising one sulfur and two nitrogen atoms that are responsible for its basic and electron-deficient character along with a relatively easy introduction of structural modifications (in the form of external substituents) in carbon positions[15]. Driven by the exceptional biological activity of this group of compounds, including antibacterial, antifungal, antimicrobial, antiviral, anticancer, antioxidant and anti-inflammatory properties, good electron-accepting ability, and thermal and chemical stability, numerous thiadiazole derivatives have been developed so far and applied widely in pharmaceutics, agriculture, and materials chemistry as drugs, agrochemicals, and potent inhibitors against corrosion of metals and alloys[15–18]. From the perspective of the development of new functional materials, also the optical end emission features exhibited by thiadiazoles are equally interesting, such as strong fluorescence that can be quenched or enhanced by a metal ion binding affording chemisensing ability[19–22], photoluminescence caused by photoinduced inter- and intramolecular charge transfer[23–29]excited-state intramolecular proton transfer (ESIPT) phototautomerization[29–34], and aggregation-induced emission (AIE) or AIE enhancement (AIEE)[29,35–40], often resulting in appearance of dual emission.

The dual emission phenomenon occurs as an effect of co-existence of two (or more) emissive excited states in a system, and depending on their origin it might be classified as arising from one emitter with two emitting states, two independent emitters or two emitters that are correlated[41–43]. Among many established mechanisms of dual emission, the most common ones involve simultaneous appearance of both fluorescence and phosphorescence in one emitter due to efficient intersystem crossing between singlet and triplet excited states or occurrence of two fluorescence signal via violation of the Kasha's rule, thermally activated (delayed) fluorescence, intramolecular charge-transfer effects, or aforementioned ESIPT and aggregation effects including also co-existence of both non-aggregated and aggregated species. Compounds that display dual emission show a high potential in practical optoelectronic and biomedical applications such as in organic light-emitting diode devices, anticounterfeiting, encryption and data storage, sensor construction and cell imaging[42,43]. Interestingly, many systems capable of producing the effect of dual fluorescence also show relatively good microbiological properties (indeed, often better than other analogues from a given group of compounds)[44,45]. While the phenomenon itself cannot explain microbiological characteristics, it is often related thereto, as indicated, for example, by the relevance of concentration-related effects. Furthermore, more importantly, the effect can be used to develop potentially very effective molecular probes capable of detecting even the slightest environmental changes (given that the underlying effects such as ESIPT or AIE are particularly sensitive to changes in the medium). Taking into account this wide range of possible applications, there is still a need to design and modulate novel dual-fluorescent materials that would demonstrate good stability and high efficiency. This can be achieved by e.g. embedding emitters into rigid environments such as polymer hosts[46–48].

The presented studies explore physical and photophysical properties of starch-based biopolymer films containing a powder of a simple 1,3,4-thiadiazole derivative of potential pharmacological activity, 5-(4-nitrophenyl)−1,3,4-thiadiazol-2-amine (NTA, Fig. 1), used as a nanofiller. Physicochemical characteristics of the prepared material was obtained by means of Fourier-transform infrared (FTIR) spectroscopy, atomic force microscopy (AFM) and color measurements and complemented by an in-depth analysis of its photophysical properties examined with stationary absorption spectroscopy, fluorescence spectroscopy (with resonance light scattering, RLS), fluorescence anisotropy measurements as well as time-correlated single photon counting (TCSPC). To shed light on the mechanism of the dual fluorescence phenomenon observed in starch/NTA films, additional measurements (including concentration-dependent emission experiments) were also performed for pristine NTA in propan-2-ol solution, complemented by single crystal X-ray diffraction examination and (time-dependent) density functional theory ((TD)DFT) calculations on both monomeric and aggregated (dimer and trimer) forms of the compound. The presented research has been envisioned to be of fundamental character, aimed at proposing a (first) chromophoric additive to pure starch, rather than engineering the system into a working material.

Results and discussion

The considered biopolymer films were prepared using the potato starch as a raw material, glycerol as a plasticizer to increase the flexibility and plasticity of the film, and 5-(4- nitrophenyl)−1,3,4-thiadiazol-2-amine (NTA, Fig. 1a) powder as a functional nanofiller. The samples were prepared with 20% glycerol and, to examine the influence of the NTA additive on the material properties, with the addition of 0% (0.000 g), 0,175% (0.007 g), 0.35% (0.014 g), and 0.7% (0.028 g) of NTA relative to the starch dry matter. In the following, the corresponding samples are referred to as T0 (= control), T1, T2, and T3, respectively.

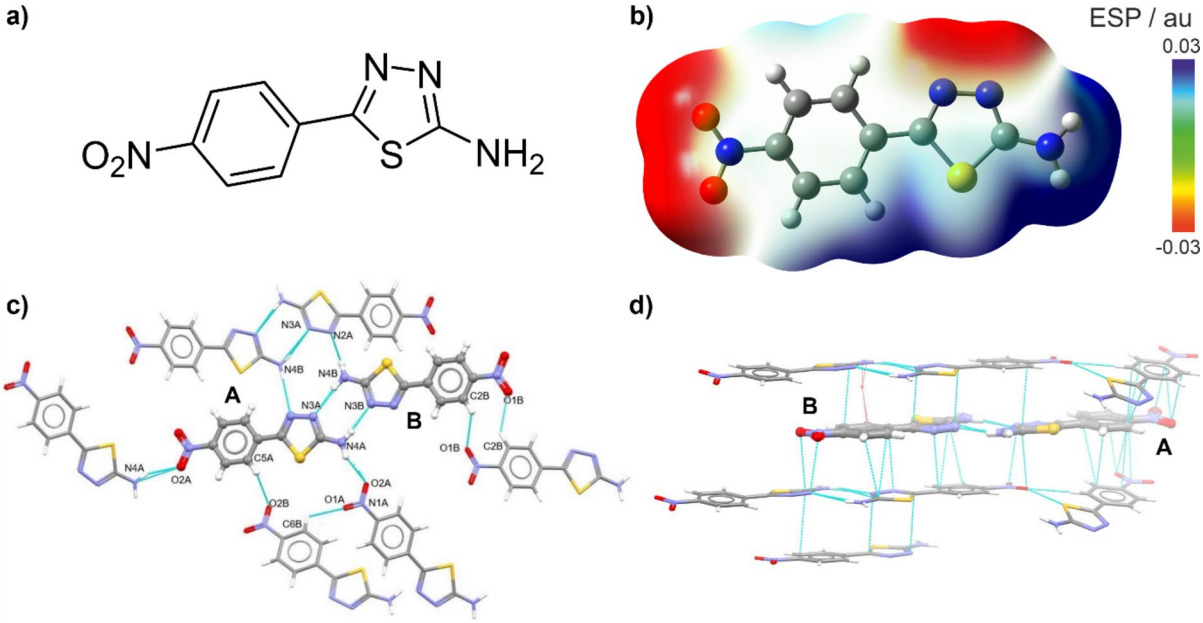

Fig. 1. Schematic structure of NTA molecule (panel **a**) along with its electrostatic potential (ESP) mapped onto electron density isosurface (0.0004 au) as computed with B3LYP + D3/6-31 + + G(d, p)/PCM(2-propanol) with electron-deficient/electron-rich regions codded as blue/red (panel **b**). Intermolecular interactions stabilizing NTA X-ray crystal structure: hydrogen bonds (panel **c**) and π···π stacking (panel **d**).

Crystallographic characterization of NTA

NTA is a simple, yet interesting photoactive 1,3,4-thiadiazole derivative, consisting of two aromatic rings: 4-nitrophenyl and 1,3,4-thiadiazole amine (Fig. 1a). Single-crystal X-ray diffraction measurements show that the compound crystallizes in the orthorhombic crystal system in the Pbcn space group with two molecules (A and B) in the asymmetric part of a unit cell (see Fig. 1 and Figure S1.4 in Supplementary Materials). The structure of NTA is primarily stabilized by intermolecular hydrogen bonding and π···π stacking interactions, the former nicely reflecting the computed molecular electrostatic potential (ESP) map demonstrating electron-rich (marked in red in Fig. 1b: thiadiazole nitrogen and nitro group oxygen atoms) and electron-deficient sides (marked in blue: amino group and phenyl hydrogen atoms), representing respectively hydrogen bond acceptors and donors. Specifically, molecules A and B form an almost planar dimer via two strong N-H···N hydrogen bonds between the nitrogen atoms from the thiadiazole rings and amino groups (N1A-H1A···N3B and N4BA-H4BA···N3A in Fig. 1c; see Table S1.2 for geometrical details). According to calculations performed in CrystalExplorer70, this dimer exhibits the lowest energy (−80 kJ/mol) among other motifs. The two dimers are connected via hydrogen bonding (N4B-H4B···N2A) to form tetramers, in which interaction energy between dimers was estimated to be −35 kJ/mol. In addition to the N-H···N hydrogen bonds, N-H···O interactions (between the amino and nitro group: N4A-H4AB···O2A) and C-H···O interactions involving two phenyl rings can also be observed in the NTA crystal structure. Molecules related via N4A-H4AB···O2A hydrogen bonds form infinite chains. As molecules are planar and aromatic, the π···π stacking interactions appear in the direction perpendicular to the plane of the molecule (see Fig. 1d). The strength of such interactions is comparable to that of hydrogen bonding with two hydrogen-bonded dimers interacting via π···π stacking interaction energies equal to ca. −36 kJ/mol. The packing of molecules is presented in Figure S1.5. In direction a, typical herringbone motif that appears when molecules are aromatic and interact via π···π stacking can be seen, in direction b, infinite chains appear. The tendency of NTA to form multiple hydrogen bonds, clearly shown in its X-ray crystal structure, was therefore identified as a possible path to incorporate this system into a starch/glycerol-based material, furnishing it with novel photophysical functions.

Structural analysis of starch/NTA biofilms via ATR-FTIR spectroscopy

ATR-FTIR spectroscopy is a very powerful tool facilitating elementary analysis of various types of organic compounds and materials containing, for instance, biodegradable film components such as starch. Moreover, it can be used to detect possible interactions between film components and 1,3,4-thiadiazole additives, while the characteristic peak spectrum could reflect the effect of physical and chemical interactions[49]. The applicability of FTIR in establishing the content of compounds in materials exhibiting biodegradable properties has been confirmed in a growing body of studies, including our own, as reported in literature[50]. Starch materials reveal very intense and interesting IR bands due to their content of carbohydrates and plant polysaccharides. They comprise mainly glucose units linked by α glycosidic bonds. There are two main fractions, the first being unbranched amylose, which consists of glucose residues linked together by oxygen atoms via α−1,4-glycosidic bonds. The other component is branched amylopectin with additional α−1,6-glycosidic bonds. The incorporation of the NTA additive, which produces intense IR bands, suggests a significant modification of molecular interactions in

the obtained group of biodegradable film materials. All of these factors translate to evident changes in the FTIR spectra of the film selected for the study[50].

For a more convenient analysis of the obtained FTIR spectra, Fig. 2 shows and Table S1.3 lists all the significant vibrations as well as their association with specific functional groups present in the studied systems, assigned based on the available literature[51]. As can be seen, noticeable changes between the spectrum for the biopolymer/NTA gel and the biopolymer/NTA film are clearly visible. To facilitate the analysis, the corresponding spectra measured for the control film without any additives (grey line) and for the NTA compound powder (grey dashed line) are also provided for a comparison.

The molecular vibrations of the pristine NTA (grey dashed line in Fig. 2) are quite characteristic, featuring the NH_2stretching vibrations with the maxima at 3417 and 3345 cm^{-1}, likely enhanced by the C–H stretching modes. The maxima at 3278 and 3090 cm^{-1}correspond to the stretching vibrations of C–H, which may also overlap with the associated N–H stretching region extending further down to 2670 cm^{-1}. The maxima at 1639 and 1621 cm^{-1} are attributed to the C=N stretching and N–H deformation vibrations, reinforced by the asymmetric stretching vibrations of NO_2groups. The peak at 1621 cm^{-1}may also be enhanced by the neighboring C=C stretching vibrations, which predominantly appear with maxima at 1448 and 1403 cm^{-1}. The regions from 1590 to 1490 $cm^{-1}$and from 1380 to 1260 cm^{-1}correspond to the N–H and the C–H deformation vibrations, respectively. the subsequent peaks at 1177 and 1126 $cm^{-1}$are associated with the C–C stretching modes. Finally, the region below 1010 cm^{-1}down to 600 cm^{-1} comprises the C–H deformation vibrations.

The ATR-FTIR spectrum of the control biopolymer film (grey line in Fig. 2) shows the characteristic broad band in the wavenumber range of 3550–3100 cm^{-1}corresponding to the stretching vibrations of the –OH group of the free, internal, and external molecular hydrogen bonds occurring in the starch structure[51]. The tested sample contained a low content of water molecules, which manifested itself by the presence of faintly intense bands in the region around 1650 cm^{-1}, representing the deformation vibrations of –OH. Another noteworthy vibration ranges include: (i) of 3000–2700 cm^{-1}, characteristic of the symmetric and asymmetric C–H stretching vibrations in the –CH2 groups[49], and (ii) of 1200–1000 cm^{-1}, comprising the C–O stretching vibrations originating from the C–O–C groups and naturally occurring in polysaccharides. In contrast, the area from 930 to approx. 700 $cm^{-1}$is characteristic of vibrations of the polysaccharide ring, with vibrations falling under this range ascribed to the pyranose ring in individual units corresponding to a single glucose unit[52].

In the FTIR spectrum of the starch/NTA gel consisting of an aqueous biopolymer solution combined with a NTA solution in isopropyl alcohol (black dashed line in Fig. 2), the characteristic peak at 3310 $cm^{-1}$is mainly associated with the presence of hydroxyl groups from the gel medium and of NH2 groups from the NTA compound, and its broad form may also result from an increase in the number of hydrogen bonds formed in such system between the NTA, biopolymer and solvent molecules. The vibrations observed at 3000–2800 cm^{-1}correspond to the C–H stretching originating from CH groups. Surprisingly, we do not observe the associated N–H stretching vibrations, which may be related to the interaction of the compound with the biopolymer structure. The peak centered at 1650 $cm^{-1}$is due to vibrations involving the –OH groups from the medium, and the C=N, C=C, N–H, and NO2 groups present in the NTA compound. The bands at 1458, 1382 and 1417 cm^{-1} can be related to the bending vibrations from C–H and the stretching vibrations from C=C groups.

As shown in Fig. 2, the FTIR spectrum obtained for the starch/NTA biopolymer film (black line) visibly differs from that of the gel, with some peaks shifted towards lower or higher frequencies and altered bands intensities, but on the other hand it highly resembles that of the control film. In particular, the strong absorption peak observed for the starch/NTA gel at 3310 cm^{-1}has a larger and wider wavenumber range and higher intensity than those measured for the starch/NTA and control films (3303 cm^{-1}), the latter two differing only in the band

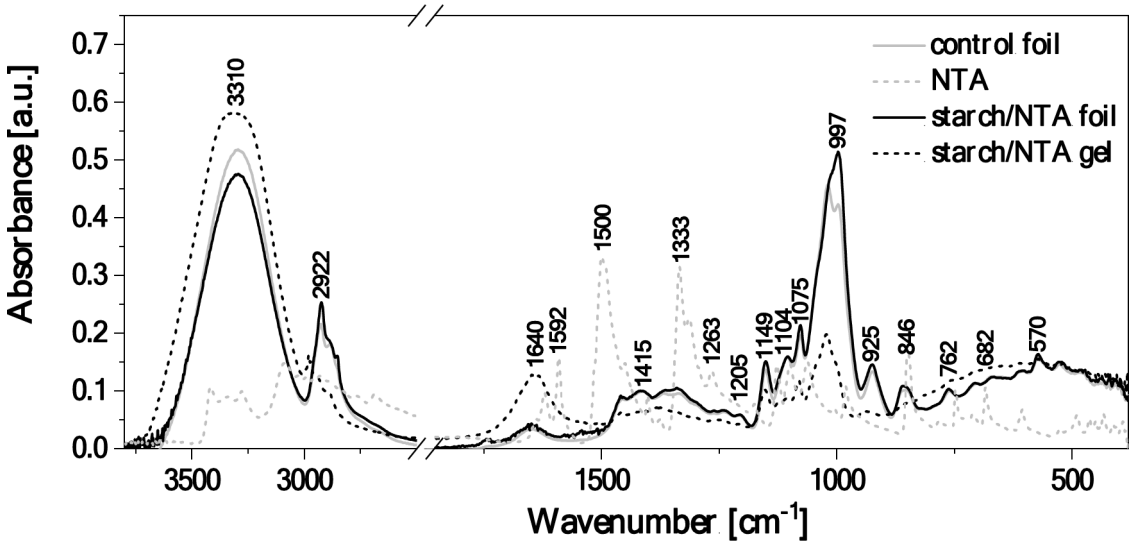

Fig. 2. 5 ATR-FTIR absorption spectra of the starch/NTA gel and starch/NTA film, and of the control biopolymer film and the NTA powder as reference systems.

intensity, which decreases upon thiadiazole addition. The shift towards lower frequencies and the observed peak width and intensity alternations reflect the absence of solvent molecules in the films (compared to the gel) and the resulting rearrangement of intermolecular hydrogen bonding interactions, which in the biopolymer/NTA film will now involve mainly starch and thiadiazole molecules[52], and thus likely differ from intra- and intermolecular hydrogen bond network present in starch itself. Moreover, the signal at 1640 $cm^{-1}$for the gel (attributed, among others, to vibrations of –OH groups from the medium) shifts to ca. 1648 cm^{-1} and decreases significantly in the biopolymer film, which may indicate that the amount of unbound OH groups is notably lower in the biopolymer material. A subtle band with a maximum at ca. 1550 cm^{-1} can be indicative of vibrations from the NTA NO_2groups. Finally, very profound changes between the FTIR results for the starch/NTA gel and for the starch/NTA film were also observed in bands with peaks at around 1060–950 $cm^{-1}$with the greatly intensified signal for the latter case. This is not unexpected, as the fingerprints of the skeletal vibrations of the C–O and C–C groups, which are typical of starch, occur in this spectral region[52], and they may be reinforced by vibrations originating in the additives[53]that indeed accounts for the higher intensity of the peak at ca. 1000 cm^{-1} for the film with the thiadiazole vs. the control one.

In summary, the comparative analysis of the FTIR spectra obtained for the starch/NTA gel, the starch control film and the starch/NTA film appears to indicate an effective and uniform incorporation of the thiadiazole additive into the biopolymer material occurring via, for example, hydrogen bonding interactions between NTA and starch molecules. Indeed, quantum-chemical calculations performed for some possible NTA complexes with α-D-glucose (the starch basic building unit) and with a truncated amylopectin molecule (one of the two starch components) support the existence of a plethora of possible binding sites between NTA and starch biopolymer based on hydrogen-bonding and CH-π interactions (see Figures S2.8 and S2.9).

Surface characterization of starch/NTA biofilms

Surface properties parameters obtained from the AFM measurements are presented numerically in Table 1 and in the form of representative maps of height, Derjaguin–Muller–Toporov modulus, and adhesion force in Fig. 3. It can be observed that the addition of NTA 1,3,4-thiadiazole derivative does not significantly affect the roughness of the starch film's surfaces. The root mean square roughness parameter Sq for the films tested remains within a narrow range, with the T3 sample (of the highest NTA content) measuring at 70.7 nm and T2 at 79.7 nm. Likewise, a similar trend is observed in the surface roughness parameter Sa, for which the lowest value of 53 nm was obtained for the T3 and the highest of 63.3 nm for the T2 sample. The determined surface DMT Young's modulus for all examined films reached similar values, indicating no significant effect of the 1,3,4-thiadiazole on the surface stiffness; the minimum value of the modulus was measured for the T1 film (358 MPa) and the highest for T3 (464 MPa) thus showing its slight increase with the increase of the NTA content in the film.

The adhesion parameter describes the interaction force between the surface of the film and the microscope's scanning probe. Considering the film's application, the value of the adhesion force of a given surface affect, among other aspects, wetting properties for various types of liquids or interactions with different types of polar solids. The results obtained for the considered films demonstrate that the addition of the NTA 1,3,4-thiadiazole additive into the starch biopolymer appears not to affect the adhesion strength value, as all the determined values were in the narrow range of 2.61 nm to 2.93 nm. In line with the adhesion force results, the differences in the contact angle values depending on the percentage of the NTA content are also not significant. The surfaces of all the films are characterized by similar high wettability, i.e., hydrophilicity (54°–59°). Any minor differences could have resulted from the surface morphology, on which a given drop was deposited.

Finally, a colorimeter measurement was also carried out to assess the influence of the additive on the color of the obtained biocomposite films; the outcomes are presented in Table 1. NTA powder exhibits a highly pronounced yellow color. Thus, it is unsurprising that its inclusion in a colorless film would impact a coloration effect. This is confirmed by the obtained values of the a* and b* parameters, which indicate directional changes in the color CIE L*a*b* space towards yellow. The L parameters for all the modified films decrease as the additive increases, making the films less bright. Parameter C describes low color saturation; in this case, increasing the

	T0	T1	T2	T3
NTA content (g)	0.00	0.007	0.014	0.028
Sq (nm)	75.1 ± 23	73.6 ± 10	79.7 ± 36	70.7 ± 8
Sa (nm)	55.2 ± 16	57 ± 8	63.3 ± 30	53 ± 12
DMT modulus (MPa)	383 ± 31	358 ± 54	406 ± 37	464 ± 88
Adhesion (nN)	2.93 ± 0.4	2.85 ± 0.4	2.61 ± 0.2	2.67 ± 0.3
Contact angle (°)	59.6 ± 4.1	55.2 ± 3.3	54.6 ± 4.4	55 ± 4.9
L*	93.38 ± 0.01	93.04 ± 0.40	92.59 ± 0.19	90.87 ± 0.15
a*	−0.49 ± 0.10	−3.59 ± 0.09	−3.55 ± 0.26	−2.74 ± 0.22
b*	3.45 ± 0.28	11.43 ± 0.28	17.04 ± 0.26	27.95 ± 0.20
C	1.2 ± 0.25	9.61 ± 0.29	15.05 ± 0.28	25.76 ± 0.26
H	−1.43 ± 0.02	−1.27 ± 0.0	−1.37 ± 0.01	1.47 ± 0.01

Table 1. Values of surface mechanical parameters and contact angle along with CIE L*a*b*, chroma and hue parameters determined for the examined biofilm samples differing in the NTA content. Data given as: mean ± standard deviation.

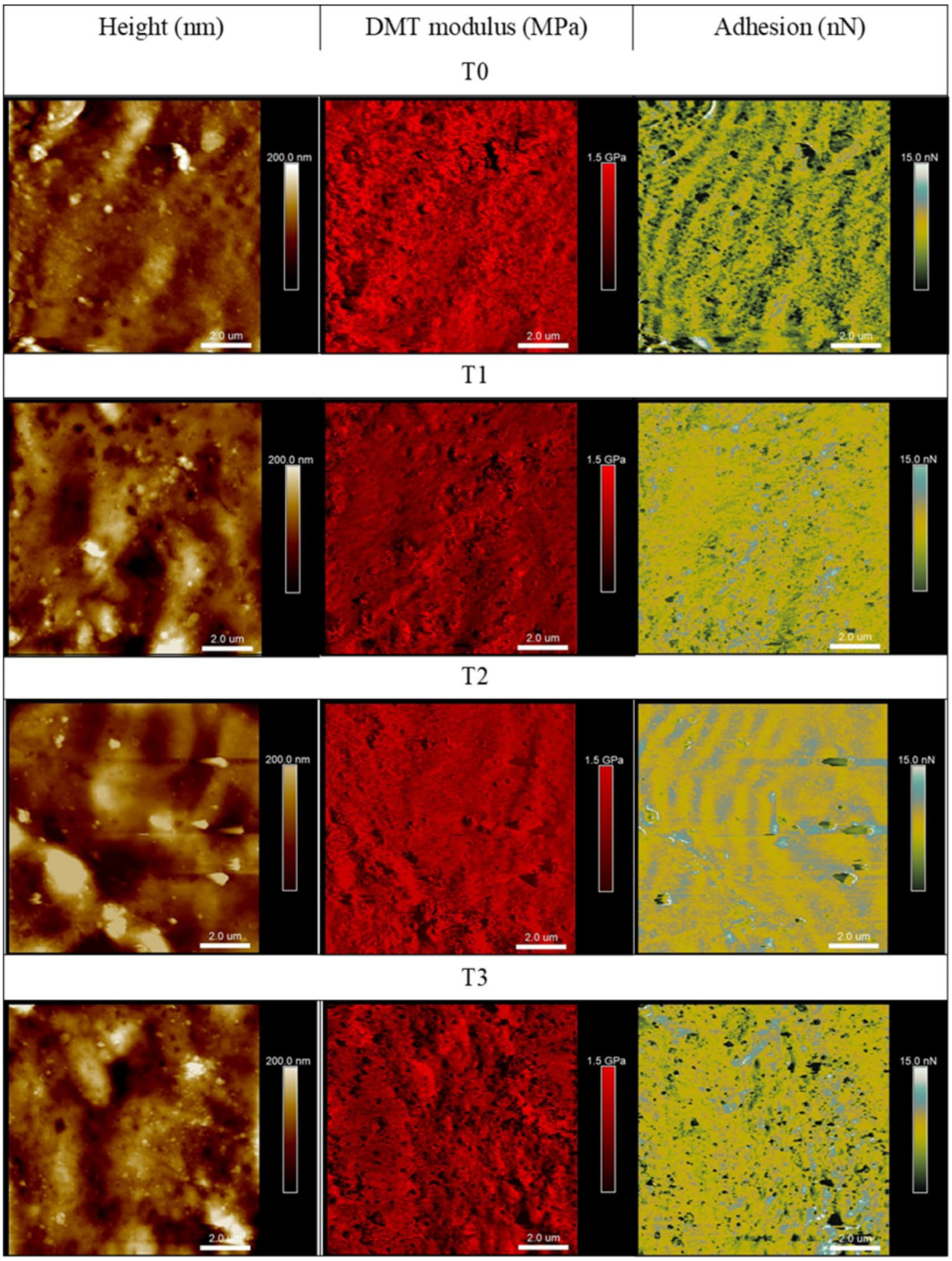

Fig. 3. Representative AFM maps (10 μm × 10 μm) of topography, DMT modulus and adhesion obtained for the examined biofilm samples differing in the NTA content.

additive leads to an increase in color saturation, particularly in the case of yellow. However, regardless of the additive, the measured values of H, indicative of hue, remain relatively stable around or slightly below 0 for all the film samples. This observation means that there are no significant changes in the hue of the film depending on the NTA additive concentrations.

Concluding, all these data indicate that NTA primarily influenced the films' color without substantially altering their surface properties.

Photophysical properties of starch/NTA biofilms

With the anticipation that blending of commonly photoactive 1,3,4-thiadiazole derivative with a starch biopolymer can furnish it with additional optical functions, photophysical properties of the prepared starch/

NTA films were finally examined and analyzed comparatively with respect to the results measured also for the starch/NTA gel and the pristine NTA in propan-2-ol (PrOH) and glycerin solutions. Naturally, one should underline the often-neglected fact that a direct comparison of the results for films with those obtained in solvent systems is not straightforward and undoubtedly challenging; it may however provide a valuable insight into spectroscopic properties of a system in question. The corresponding electronic absorption and fluorescence spectra obtained for all the systems are presented in Fig. 4.

As can be seen in Fig. 4a, for all the considered systems (NTA in PrOH and glycerin, starch/NTA in the form of a solid gel from which subsequently the biopolymer matrix was obtained, and starch/NTA biopolymer film), a wide UV-Vis absorption band was observed within the spectral range from ca. 285 nm to 435 nm, with the maximum at ca. 340–352 nm, while the starch control film showed, as expected, negligible absorption in the considered wavelengths range. The dominant signal, according to literature data and supported here by quantum-chemical calculations (vide infra), is characteristic of the $\pi \rightarrow \pi^*$ electronic transition in the given thiadiazole-based chromophore, and its energetic position appears to undergo a fairly substantial hypsochromic shift (blue-shift) from 352 nm to 340 nm when changing the NTA medium from solution to gel; a rather negligible blue shift of 2 nm is observed for the starch/NTA film vs. NTA in PrOH. This is in line with the results of the colorimeter measurements of the films presented above. Interestingly, for both the starch/NTA gel and the film, a widening of the dominant low-energy absorption band on the longwave side is visible, which may be a preliminary indication of the presence of aggregation effects such as the formation of NTA dimers or larger aggregates[44].

Contrary to the visible but overall modest changes in the electronic absorption, a much more substantial effect of the medium in the considered systems can be seen when comparing their corresponding emission spectra (Fig. 4b; for all the samples, the measurements were performed with the excitation wavelength of 350 nm, i.e. the maximum of the absorption band). Specifically, for the NTA PrOH solution and starch/NTA gel, a rather weak fluorescence emission with a clear maximum at 410–430 nm was observed, widened on the longwave side at ca. 530 nm in the former case (PrOH solvent) and uniformly visibly quenched in the latter (gel). In glycerin, practically only a single emission with the maximum at ca. 420 nm appeared, visibly more intense than in propanol. Conversely, the incorporation of NTA into the starch polymer matrix, to our delight, resulted in a significantly enhanced (ca. five times more intense) and a very clear double fluorescence signal with the shortwave band maximum at ca. 430 nm and the longwave one at ca. 530 nm. Interestingly, it can be noted that combining the starch biopolymer and the NTA additive not only triggered the interesting dual emission phenomenon in the starch material, but also visibly changed the internal fluorescence characteristics of the NTA compound itself.

Restriction of molecular movements including intramolecular rotations by surrounding biopolymer chains can significantly enhance the fluorescence emission efficiency and thus its intensity for small organic molecules such as the studied 1,3,4-thiadiazole, significantly limiting other deactivation pathways of the excited state. With this in mind, the impact of the NTA concentration in the starch biopolymer matrix on its emission was then examined. The fluorescence emission spectra recorded for three starch/NTA film samples differing in the NTA content are plotted in Figure S1.6, showing in each case a clear effect of dual fluorescence with a shortwave / longwave band centered at ca. 430 nm / 535 nm. Interestingly, while a visible increase in intensity of the emission signal was observed when increasing the concentration of NTA in the sample from T1 to T2 (with more a pronounced effect for the higher-energy band), a further increase in the additive content led to its decrease to the level recorded for T1.

To shed some light on the origin of the dual fluorescence effect observed for the starch/NTA films, the corresponding fluorescence excitation, RLS and fluorescence anisotropy spectra were then measured and

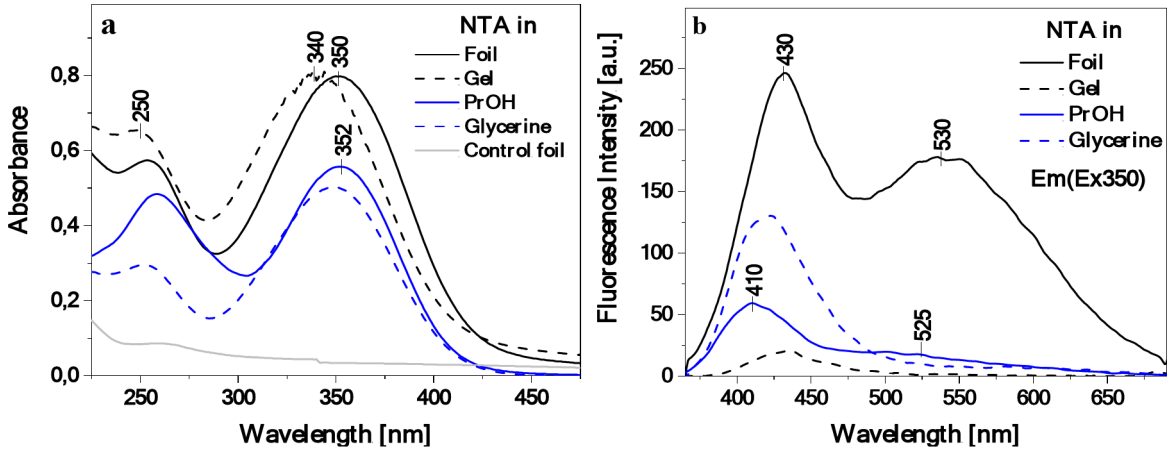

Fig. 4. Electronic absorption spectra for NTA in isopropanol and glycerin (C $4.5 \cdot 10^{-5}$) solutions as well as for starch/NTA gel and starch/NTA film (T2 sample) (panel **a**) along with the corresponding fluorescence emission spectra after excitation at the wavelength of 350 nm (panel **b**). Absorption of the starch control film is also shown for a comparison in panel a.

analyzed. Figure 5 presents the fluorescence excitation spectra (Ex) for the considered systems (NTA in PrOH and glycerin solution, and starch/NTA biopolymer gel and film representing the T2 sample), registered at wavelengths corresponding to the maxima of the respective fluorescence emission spectra shown in Fig. 4b, i.e. at ca. 410–430 nm and 530 nm. Significantly higher sensitivity and selectivity of such spectra as compared to electronic absorption allows for direct observation of excitation of a specific molecular form, e.g. monomers or aggregates in a given system[44]. Indeed, the Ex spectra followed the emission wavelength of 410 nm (NTA in PrOH), 420 nm (in glycerin), and 430 nm (starch/NTA gel and biofilms), plotted in Fig. 5a, demonstrated the single band in the spectral region from 265 to 370 nm with the maximum at ca. 295 nm for gel and ca. 325 nm for PrOH and glycerin solution and for films, whereas the corresponding measurements followed the emission wavelength of 530 nm (Fig. 5b) showed either practically no signal (gel) or the relatively intense band between ca. 300 and 450 nm with the maximum at ca. 390 nm and a clear shoulder on the short-wavelength side of the spectrum at ca. 330–350 nm. As follows from literature[54–56], the excitation band for the shortwave emission can be considered as corresponding to the monomeric form of NTA, while the broad asymmetric band for the longwave emission appears to be characteristic of aggregated species. Further evidence of aggregation effects is provided by the measured RLS spectra (Fig. 6), which for the starch/NTA gel and biofilm samples (in the latter case in the entire spectral range considered) showed intense bands of oscillatory structure, indicative of the formation of the aggregates of different geometries and sizes[57–59]. It should be noted that the RLS spectrum for the diluted solution of NTA in PrOH demonstrated very low intensity; it had to be increased tenfold to be visible in Fig. 6. Interestingly, the RLS spectrum of low but non-negligible intensity was recorded for NTA in the glycerin solution, which, given the fact that NTA in this medium showed a single emission (compare with Fig. 4b), indicates that non-emissive aggregates have to be formed in this case[60]. Similar results to those presented in Figs. 5 and 6 for the T2 starch/NTA film were also obtained for other prepared samples with the lower (T1) and higher (T3) NTA content (see Figures S1.7 and Figures S1.8), which evidenced the existence of aggregated forms in the analyzed system, even at relatively low concentrations of the thiadiazole compound. Finally, Fig. 7presents the fluorescence anisotropy spectra measured for NTA in PrOH and for the considered biofilms. In the case of the latter, a relatively high level of anisotropy was revealed, from ca. 0.3 in the shortwave to ca. 0.2–0.25 in the longwave emission range, which tends to be characteristic of solidified systems[76]. Notably, while in the wavelength range of ca. 430 nm, associated with the first fluorescence emission band, rather low anisotropy was measured (ca. 0.05) for the sample of NTA in PrOH, its significant increase (to ca. 0.18–0.2) was observed in the longwave spectral range of ca. 530 nm, indicating non-negligible aggregation effects occurring also in the NTA solution.

The results presented above clearly indicate the AIE-origin of the dual fluorescence effect observed for the prepared starch/NTA biopolymer films. To further support this conclusion, concentration-dependent measurements of the photophysical properties of NTA in isopropanol were performed to follow up on the fact that a longwave band enhancement was already visible in the emission spectrum of the diluted NTA solution (Fig. 4b). The results obtained for a series of samples of NTA dissolved in PrOH, carefully titrated to increase an overall concentration of the compound in the solvent (addition from 2 to 30 µl of NTA/PrOH solution translating to the concentration ranging from 3·10–6 to 1.5·10–4), are shown in Fig. 8. As can be seen in Fig. 8a, the resulting electronic absorption spectra showed that the wide absorption band already described in Fig. 4a of systematically increased in intensity with the growing content of NTA in the solution. Similarly, as the concentration of thiadiazole increased, the expected effect of the enhanced intensity of the shortwave band maximum in the emission spectrum was observed, but additionally accompanied by a very clear increase in the longwave band intensity (Fig. 8b) reflecting the findings for the starch/NTA biopolymer films. As presented in Fig. 8c, the relationship between the ratio of the intensity at the shortwave and longwave emission band

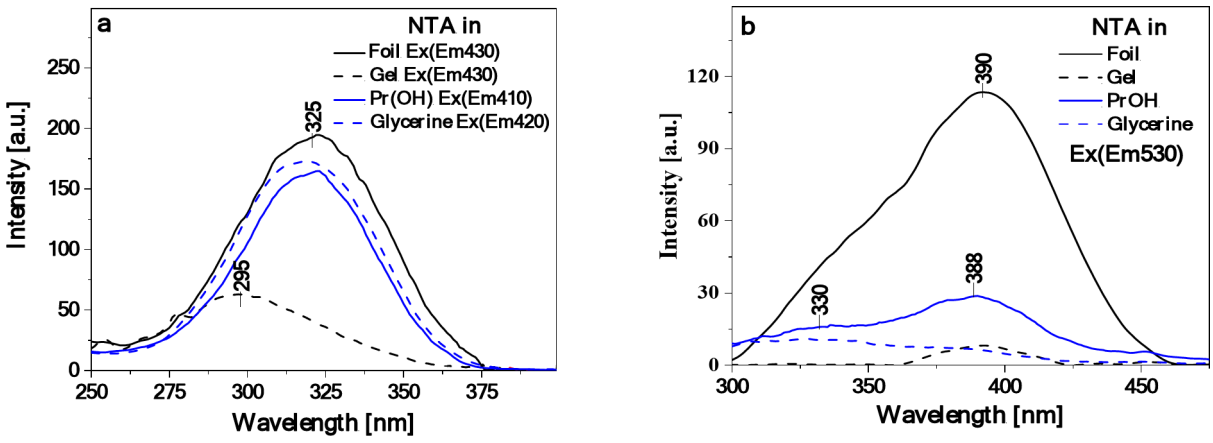

Fig. 5. Fluorescence excitation spectra of NTA in PrOH and glycerin solutions (C $4.5 \cdot 10^{-5}$) followed the emission wavelength of respectively 410 nm and 420 nm as well as of starch/NTA gel and film (T2 sample) followed the emission wavelength of 430 nm (panel **a**). In panel (**b**), the corresponding excitation spectra for the four systems followed the emission wavelength of 530 nm are presented. See Figure S1.7 for the results of analogous measurements for the starch/NTA samples with different NTA content.

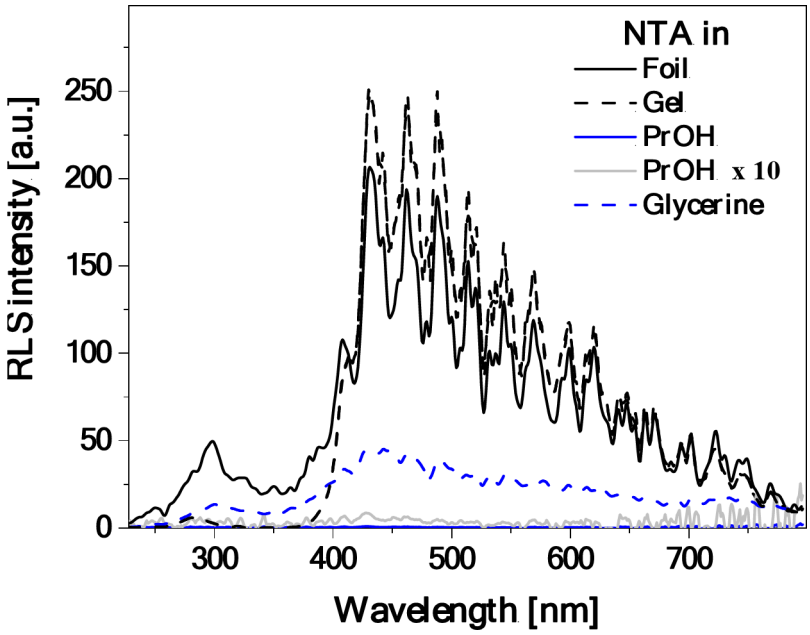

Fig. 6. RLS spectra for NTA in PrOH and glycerin solutions (C $4.5 \cdot 10^{-5}$) as well as for starch/NTA biopolymer gel and film (T2 sample). See Figure S1.8 for the results of analogous measurements for the starch/NTA samples with different NTA content.

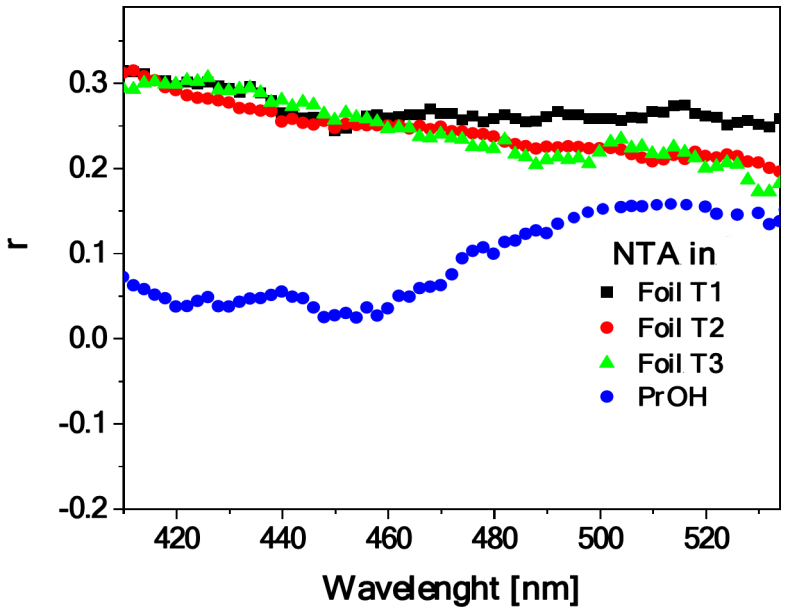

Fig. 7. Fluorescence anisotropy spectra of NTA in PrOH solution (C $4.5 \cdot 10^{-5}$) and starch/NTA biopolymer films prepared with different NTA content (T1, T2, T3 samples). Em(Ex350) - emission at 350 nm excitation.

maxima and the changes in the compound's concentration nicely illustrates this effect of the longwave signal elevation. Finally, Fig. 8d presents the RLS spectra registered for NTA in PrOH as the compound's concentration increased. It should be noted that with the growing NTA content, the intensity of the RLS spectrum increased on the longwave side but decreased on the shortwave side. All these spectral features observed for NTA in PrOH with the growing concentration of the compound in solution, mirroring the results for the starch/NTA biofilms, confirm that the appearance of the longwave emission signal constituting dual fluorescence phenomenon for NTA stems from the emergence of various aggregated structures that may differ in size.

Finally, in the subsequent part of the study related to the mechanism of molecular interactions producing the fluorescence effects observed in the emission spectra presented above, the fluorescence lifetimes were determined with the use of the TCSPC technique, in starch/NTA film (T2 sample) positioned at the magic angle

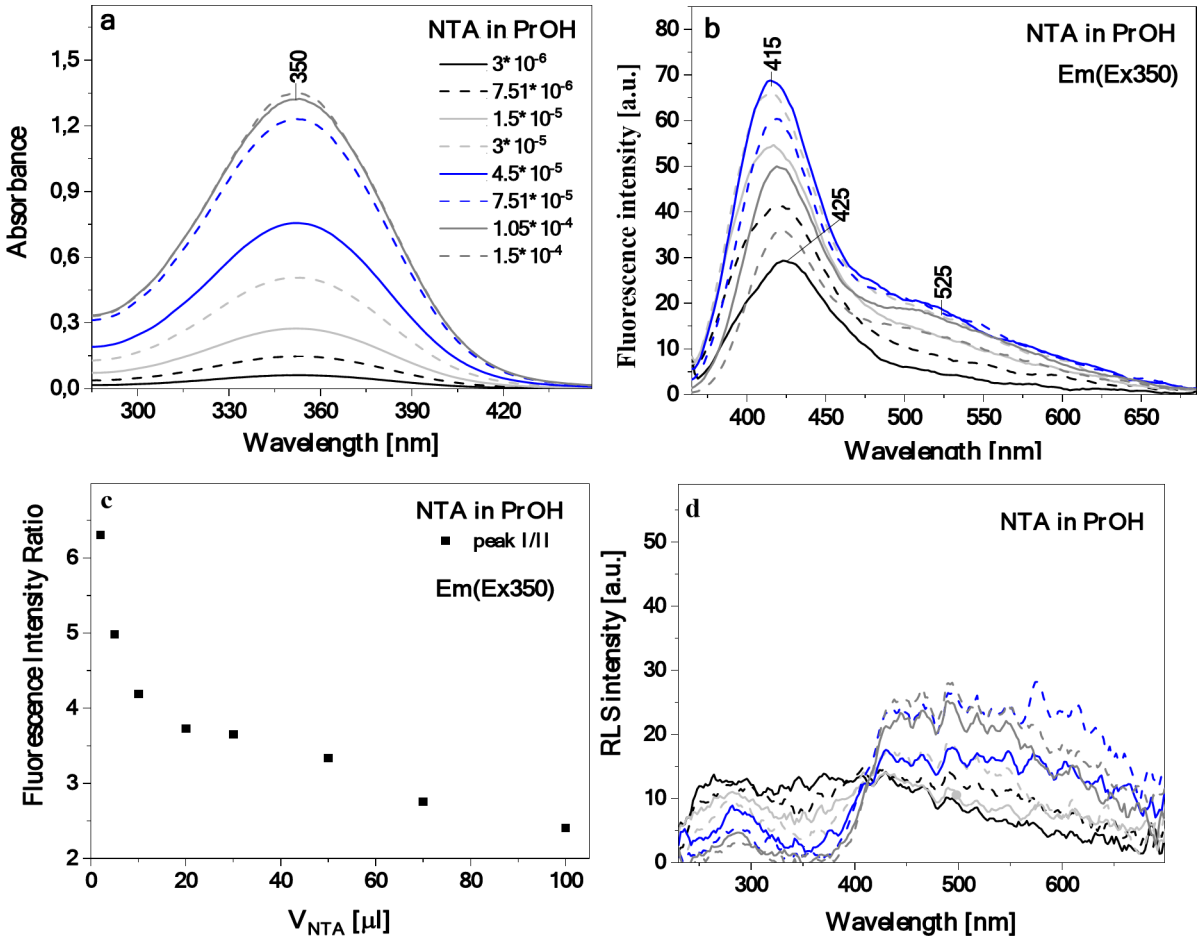

Fig. 8. Concentration-dependent electronic absorption (panel **a**), fluorescence emission after excitation at the wavelength of 350 nm (panel **b**) and RLS spectra (panel **d**) of NTA in PrOH. In panel (**c**), the relationship between ratio of fluorescence emission intensity measured at ca. 415 nm and at 525 nm and concentration of NTA in PrOH (as volume of NTA added) is presented.

as well as in two NTA PrOH solutions with concentrations of 3 µM and 150 µM. The relevant methodology is described in the Materials and Methods section. The presented data were obtained for the cut-on 408 nm filter with excitation at 372 nm. The measured values of fluorescence intensity over time are shown in Fig. 9. The results were analyzed by deconvoluting the decay of fluorescence intensity. The decays obtained for the starch/NTA biofilm were best described with a two-component model (Table 2); in this case, the monoexponential model proved insufficient while the inclusion of an additional, third component did not improve the quality of the fit. Regarding the data obtained for the NTA in PrOH solution, the character of the decay was more complex, and in order to ensure a satisfactory fit, a third component had to be added; the inclusion of a fourth component did not improve the quality of the fit. The registered decays, fits and residual distributions are presented in Fig. 9, while the numerical data of the respective fluorescence lifetimes, their fractions and mean fluorescence lifetime are presented in Table 2.

The measurements performed for the NTA in PrOH solutions (with two concentrations of the analyzed compound) revealed a very short fluorescence lifetime of 30 ± 1 ps with its very high contribution of up to 80% in both cases. The other two components returned longer lifetimes. For the less concentrated sample, they were 2.11 ± 0.04 ns and 8.2 ± 0.1 ns, with respectively 14% and 8% share. The sample with the higher concentration yielded shorter lifetimes: 0.94 ± 0.06 ns and 2.79 ± 0.02 ns with respective intensity fractions of 7% and 13%. Consequently, the mean fluorescence lifetime observed when increasing the concentration of the fluorophore decreased from 0.99 ± 0.08 ns to 0.46 ± 0.03 ns. The measurements carried out for the starch/NTA biopolymer film sample did not reveal the short lifetime observed in the solution; only the two higher lifetime values similar to those obtained for the highly concentrated solution were present. The recorded lifetimes were: 0.4 ± 0.1 ns and 2.2 ± 0.1 nm, both having an equal share.

Fluorescence emission measurements performed for both the starch/NTA films and the pristine NTA in PrOH solution (Fig. 4b) showed the emergence of the dual fluorescence signal. Naturally, as already described above, the effect was considerably more efficient in the biopolymer matrix system than in the solvent. By following this line of reasoning, it can be noted that the effect of prolonging the fluorescence lifetime (as it is the case

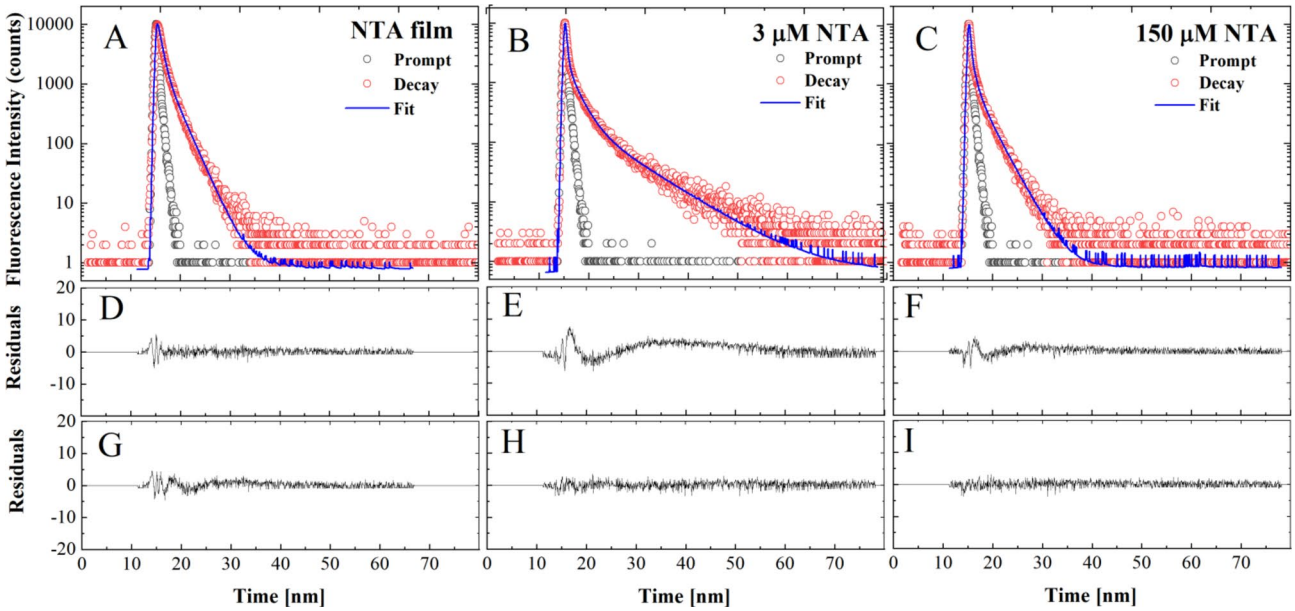

Fig. 9. Effect of different NTA content in starch film and PrOH solution on corresponding fluorescence decay. In panels (**A**, **B**, **C**), the dotted curves show the decay of fluorescence emission in the starch/NTA biopolymer and NTA solution (two concentrations) systems, while the continuous lines are the best exponential fits. Panels (**D**, **E**, **F**) demonstrate residual distributions for 2-exponential fits, and panels (**G**, **H**, **I**) – residual plots for 3-exponential fits to the data in panels A, B, C. 2-exponential fit is sufficient for the starch/NTA film (panels A, D, G), while a third lifetime component is required to describe the NTA fluorescence decay in both tested PrOH solutions.

NTA	<τ>	τ1	τ2	τ3	f1	f2	f3
$3*10^{-6}$ M	0.99 ± 0.08	0.03 ± 0.01	2.11 ± 0.04	8.2 ± 0.1	0.778 ± 0.001	0.141 ± 0.001	0.082 ± 0.01
$1{,}5*10^{-4}$ M	0.46 ± 0.03	0.03 ± 0.01	0.94 ± 0.06	2.79 ± 0.02	0.797 ± 0.001	0.071 ± 0.002	0.132 ± 0.012
Film T2	1.20 ± 0.01	0.4 ± 0.1	2.2 ± 0.1		0.5 ± 0.03	0.5 ± 0.03	

Table 2. Values of fluorescence lifetime (τ in ns) and fractional intensity (f), with their corresponding standard deviations, measured for the starch/NTA film and the NTA PrOH solutions (two concentrations). Measurements were performed using a filter with cut-on 408 nm at the excitation wavelength of 372 nm. Compare with Fig. 9.

of molecules capable of producing similar fluorescence phenomena) is characteristic of excimer interactions[44] associated with aggregation, often dimerization.

Quantum-chemical analysis of photophysical properties of NTA in its monomeric and aggregated forms

Finally, quantum-chemical (time-dependent) density functional theory ((TD)DFT) calculations were performed for NTA in its monomeric and simple aggregated (dimeric and trimeric) forms to examine how the aggregation may affect the photophysical properties of the system. Starting geometries for geometry optimizations in the ground state (DFT B3LYP + D3/6 31 + + G(d, p) with continuum solvent model for 2-propanol (PCM(PrOH))) were extracted from the X-ray crystal structure of the compound, and the resulting optimized structures of the NTA monomer, dimers, and trimer are presented in Fig. 10; see also Figure S2.1. As expected based on the crystal structure of NTA and the computed ESP map around the NTA monomer (Fig. 1b), the obtained aggregates are stabilized by intermolecular N-H···N hydrogen bonds between the nitrogen atoms from the thiadiazole rings and amino groups (as in 'end-to-end' dimer d1 and trimer) and / or π···π stacking interactions (as in parallel 'card-pack' dimers d2 and d3, and also trimer); no N-H···O interactions between the amino and nitro group were preserved during the geometry optimizations, confirming their overall lower strength. Referring to the commonly used terminology, it can be noticed that the dimers d1 and d2&d3 can be classified as respectively J-type and H-type aggregates, whereas the trimer can be considered as a so-called HJ-type aggregate[60–66]. Importantly, the negative values of the computed formation energy of these species (for d1, d2 and trimer, also after accounting for the entropy penalty) clearly confirm that they may form spontaneously. While the ground-state structures of the pristine NTA molecule and its dimeric and trimeric models presented in Fig. 10 were used to compute (TDDFT ωB97X-D/6 311 + + G(d, p)/PCM(PrOH)) vertical absorption energies and oscillator

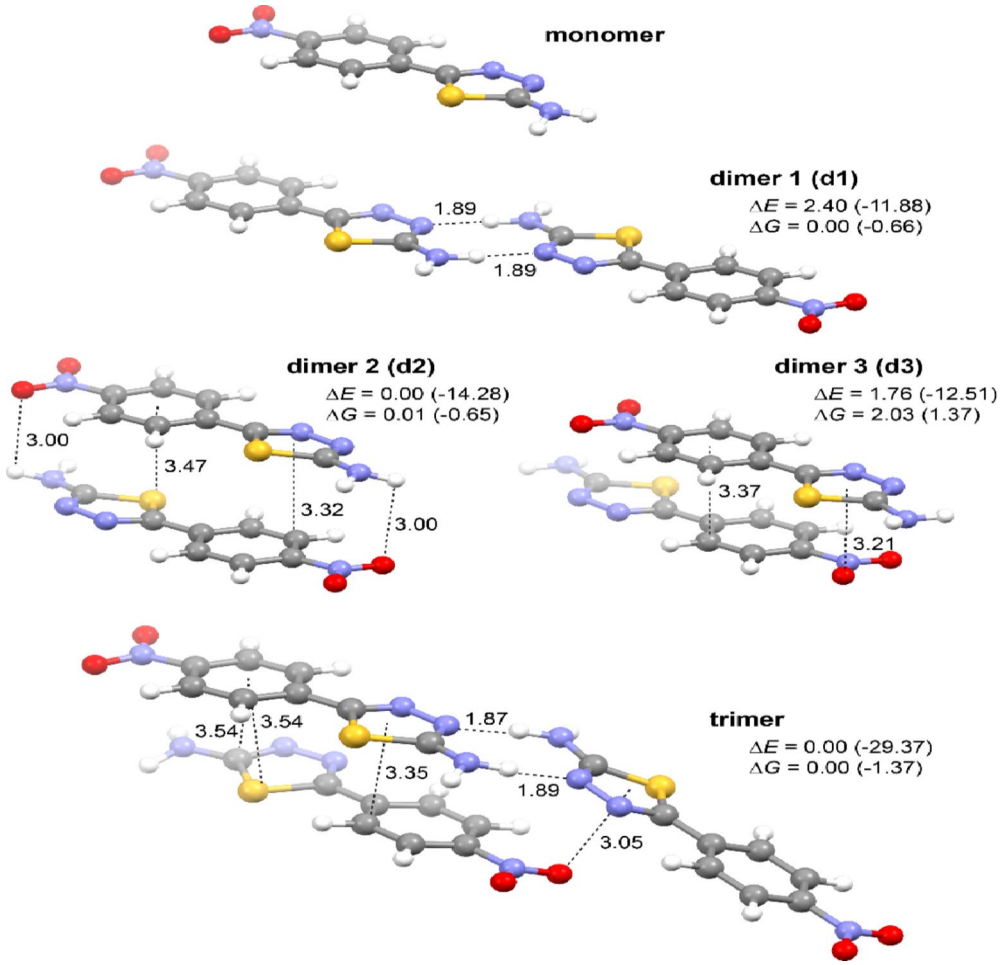

Fig. 10. Optimized (DFT-B3LYP + D3/6-31 + + G(d, p)/PCM(PrOH)) molecular structures of the monomer and aggregated models (dimers and trimer) of NTA. Values listed are hydrogen bonding and π··· π stacking (measured between the ring centroid and the closest atom in the neighboring molecule) distances (in Å) and relative energy ΔE and free energy ΔG values (in kcal/mol). In parentheses, the corresponding formation energy and free energy values are listed, computed as a difference between the energy of the aggregate and the sum of the energy of its components that is the monomer in its optimal geometry. For the structures of the aggregated models of NTA in their S1 excited state, see Figure S2.5.

strengths for the low-lying excited states to shed some light on UV-Vis properties of the compound, to model the fluorescence emission process, they were subsequently subjected to S_1 excited-state geometry optimizations. The resulting S_1 structures for the aggregates are presented in Figure S2.5 and as can be seen, they overall resemble the parent ground-state species with their corresponding 'end-to-end' and / or 'card-pack' arrangement preserved. Compared to S_0, two structural trends can be highlighted in S_1: (i) a shortening of one of the NH···N hydrogen bonds accompanied by an elongation of the other in the 'end-to-end' motifs and (ii) an overall closer distance between the molecules in the 'card-pack' structures. Moreover, unlike for the ground state, for which all the obtained dimers demonstrated rather comparable energy values, a significant preference towards the d2 form was noticed for the excited state. Finally, it should also be noted that strongly negative formation energies were determined for all the obtained S_1 aggregate models, showing that the tendency of NTA to aggregate is even more pronounced in the excited state than in the ground state.

[a] E and λ – S_1-S_0 energy difference at optimized S_0 ground-state geometry representing absorption energy; f – oscillator strength; H/L: % – percentage contribution of HOMO (H) → LUMO (L) transition to the $S_0 \rightarrow S_1$ absorption. For simulated UV-Vis spectrum, see Figure S2.2. For MOs isosurfaces visualization, see Figure S2.3. For absorption data for dimeric and trimeric forms of NTA, see Table S2.1.

[b] ΔE – relative energy value; E and λ – S_1-S_0 energy difference at optimized S1 excited-state geometry representing fluorescence energy; f – oscillator strength; H/L: % – percentage contribution of LUMO (L) → HOMO (H) transition to the $S_1 \rightarrow S_0$ emission. For S1 structures visualization, see Figure S2.5. For MOs isosurfaces visualization, see Figure S2.6.

As can be seen from Table 3, Table S2.1 and Figure S2.2, the low-energy absorption band observed experimentally at ca. 345 nm (340 nm for starch/NTA gel; 350 nm for NTA in PrOH, starch/NTA) is quite well reproduced by the calculations for both monomeric and aggregated forms of NTA with the following ππ*

excitations of sizable intensity underlying the simulated signal: $S_0 \rightarrow S_1$ for monomer and dimer d1 computed at respectively 330 and 341 nm, $S_0 \rightarrow S_2, S_5$ for dimer d2 (comp. at 333 and 322 nm), $S_0 \rightarrow S_2, S_4$ for dimer d3 (comp. at 325 and 311 nm), and $S_0 \rightarrow S_1 - S_3, S_5, S_6$ for trimer (comp. at 346, 345, 333, 326, and 324 nm). As expected, based on the spatial characteristics of the examined aggregated models, a red-shift (bathochromic shift) and a blue-shift (hypsochromic shift) of the main lowest-energy absorption peak compared to the spectrum of the pristine monomer is visible for, respectively, the J-type d1 and H-type d2&d3 dimers; a red-shift is also observed for the HJ-type trimer. Assuming that NTA aggregates of different molecular arrangements can be formed upon increasing the concentration of the compound in PrOH and upon its incorporation into the starch biopolymer matrix, which is plausible given its X-ray crystal structure based on various H-bonding and π···π stacking motifs, they will all contribute to the resulting UV-Vis absorption signal, which on average should thus accordingly be broad with the low-energy maximum close to that observed for the non-aggregated state. This is indeed observed experimentally, see Fig. 4.

The wavelength of the $S_1 \rightarrow S_0$ emission computed for the pristine monomeric NTA form (431 nm, see Table 3) almost perfectly coincides with the maximum of the fluorescence signal observed experimentally for the highly diluted sample of NTA in PrOH (425 nm, see Fig. 8b). Regarding the examined dimers, the energies of the $S_1 \rightarrow S_0$ transition either remain at the value close to that determined for the monomer (d1, 437 nm) or shift to a shorter (d3, 389 nm) or longer wavelength (d2, 536 nm) with the latter nicely corresponding to the longwave emission signal measured for NTA upon increasing its concentration in the PrOH solution (525 nm) and for starch/NTA films (530 nm, see Fig. 4b). A significant red-shift of the emission wavelength vs. the monomer was also observed for the considered trimer structure (463 nm), for which the corresponding $S_1 \rightarrow S_0$ transition additionally revealed sizable oscillator strength value (unlike for d2). Accordingly, even though the computed results should be treated only semi-quantitatively as the examined aggregates are just a few of many possible types and sizes, the performed calculations, supporting the experimental findings presented in the previous sections, clearly confirm that the dual fluorescence signal observed for the NTA either in solution or biopolymer film can be due to the coexistence of non-aggregated and various aggregated forms of NTA with the shortwave emission band, stemming from either the monomeric state or such species as e.g. hydrogen-bonded 'end-to-end' & π···π-stacking stabilized offset 'card pack' dimers, and longwave emission signal representing AIE effect via a formation of π···π-overlapped dimers and / or more complex / higher-order aggregates of likely slightly different photophysical characteristics (compare, for example, dimer d2 and trimer models) contributing to the experimentally observed wideness of this band. Further, more advanced studies, involving molecular dynamic simulations, would be needed to provide a possibly more realistic representation of NTA aggregates, fully accounting for their size polydispersity and structural variety.

Conclusions

Selection and sustainable sourcing of renewable raw materials at a rate that is commensurate with their natural replenishment is paramount for ensuring long-term availability and minimizing the negative environmental impact. Starch, a readily available, renewable, and relatively inexpensive biopolymer, mitigates the risk of raw material price fluctuations and ensures stability of supply. Biopolymers based on potato starch are safe for users due to their non-toxic and biodegradable nature. Such natural materials can thus possibly play a significant role in emission reduction strategies and environmental pollution mitigation, contributing to establishing a low-emission economy[67,68]. Despite the indisputable advantages of biopolymer materials, further research is required to address the limitations of biodegradable films compared to conventional petroleum products and to ensure new specific applications. Additionally, it is essential to identify new areas in which biopolymers can effectively replace traditional materials.

This study explores the potential of a simple, yet interesting photoactive 1,3,4-thiadiazole derivative NTA as an additive in starch-based biopolymer films. The detailed characterization of physical properties of the resulting NTA/starch materials revealed that the NTA additive primarily influences the films' color without substantially altering their surface properties including surface roughness or adhesion force; therefore, all the examined films maintain high hydrophilicity. More importantly, however, combining starch biopolymer and NTA additive leads to the emergence of dual emission with the shortwave / longwave band centered at ca. 430 nm / 535 nm, thus, not only making the material emissive but also visibly changing the internal (typically single-band) fluorescence characteristics of the NTA compound itself. The comprehensive experimental (crystallographic

Model	ΔE / kcal/mol	E / eV	λ / nm	F	H/L: %
Absorption [a]					
monomer	–	2.877	330	0.792	81.7
Fluorescence [b]					
monomer	–	2.877	431	1.112	89.7
dimer 1	10.36	2.840	437	1.189	88.7
dimer 2	0.00	2.313	536	0.013	94.5
dimer 3	15.90	3.184	389	1.560	83.8
trimer 1	–	2.342	463	0.639	90.9

Table 3. Computed (TDDFT-ωB97X-D/6 311 + + G(d, p)/PCM(PrOH)) photophysical properties of monomeric and aggregated models of NTA.

and spectroscopic) and computational studies presented above, conclusively demonstrate that the dual fluorescence effect observed in the considered system can be associated with aggregation processes with the longwave emission signal representing AIE origin via a formation of π··· π-overlapped dimers or more complex / higher-order aggregates. The presented study highlights the applicability of the NTA thiadiazole derivative as an additive to biopolymer materials, which due to furnishing them with dual-fluorescent properties, may enhance their applicational potential in optoelectronic devices, sensors, and bioimaging. Additionally, the incorporation of such systems into starch matrices can also significantly enhance their antimicrobial properties, which would be particularly beneficial for applications in food packaging, medicine, and pharmacy. Some of advantages and disadvantages of the studied material can be indeed easily pointed out. Properties such as biodegradability, non-toxicity, compostability, and availability are among its advantages. However, factors like lower mechanical strength compared to synthetic films and higher production costs represent its drawbacks. Nonetheless, it is important to note that, like most starch-based materials, these films exhibit hygroscopic properties, which can be seen as both an advantage and a disadvantage, depending on the intended applications We need to admit that to fully develop the studied material into working material further examinations have to be conducted taking into account such aspects as thermal and light stability, biodegradation rates, other mechanical properties such as tensile strength, and aforementioned microbiological (antimycotic) activity. We plan to explore these issues in our future research that will enable us to provide a more comprehensive optimization of the biopolymer's properties along with development of its real-life applications.

Materials and methods

Materials

The details of the synthesis of NTA are presented in the Supplementary Materials (Figures S1.1-S1.3). The raw material used to prepare the examined biopolymer films was potato starch produced by Melvit S.A. (Warsaw, Poland), unmodified in any chemical, physical, or enzymatic way. Distilled water was utilized as a solvent, in which the polymer solution was prepared. Glycerol 99.5% produced by Avant Performance Materials was used as the plasticizer and NTA powder as the functional nanofiller. The biopolymer films were prepared by casting. The aqueous solution of starch and plasticizer was mixed with a magnetic stirrer rotating at 250 rpm and heated up to 80 °C for 30 min. A suspension containing 10 ml isopropyl alcohol and NTA was treated with ultrasonic homogenizer for 20 s. Then, it was added to the cooled (45 °C) polymer solution and mixed again for 10 min. The resulting gel, consisting of an aqueous biopolymer solution combined with a NTA solution in isopropyl alcohol, was subjected to spectroscopic analysis. Next, the composite solution (gel) was dispensed into molds and placed in a controlled environmental chamber wherein it was allowed to remain until the solvent completely evaporated. Drying was carried out at 23 °C with a relative humidity (RH) of 50% for 4 days. The films were conditioned in a desiccator. Samples were prepared with 20% glycerol and 0% (0.000 g), 0,175% (0.007 g), 0.35% (0.014 g), and 0.7% (0.028 g) of NTA relative to the starch dry matter, respectively. For the purposes of the study the respective samples were designated as T0 (control film), T1, T2, and T3.

Single-crystal X-ray diffraction

To obtain NTA crystals, 1.3 mg of NTA powder was dissolved in 1.5 mL of propan-2-ol. The mixture was stirred on a magnetic hot plate stirrer at 349 K. After a few hours, the substance was completely dissolved, and then the mixture was slowly cooled down to 278 K. Once the temperature reached 5 °C, the cap was slightly unscrewed to allow the solvent to evaporate slowly. After a few weeks, small orange crystals appeared.

For the selected monocrystal, single-crystal X-ray diffraction data were collected using a SuperNova diffractometer controlled by the CrysAlis PRO software. The diffractometer was equipped with a Cu Kα microfocus X-ray source (λ = 1.54 Å, 50.0 kV, and 0.8 mA) and a HyPix detector. Data collection was performed at room temperature.

For data reduction, CrysAlis PRO 1.171.42.70a was used. Structure was solved by SHELXS and refined in Olex2-1.5 program. The structure was deposited in Cambridge Structural Database under the deposition number of CCDC2365661.

Attenuated total reflectance – Fourier-transform infrared (ATR-FTIR) spectroscopy

FTIR spectra were recorded using an IRSpirit FTIR spectrometer (Shimadzu, Kioto, Prefektura Kioto, Japan) equipped with a single reflection ATR accessory. The measurements were performed by placing the starch/NTA biofilm samples on a single-reflection crystal; the sample mass was approximately 1 g. Each spectrum was measured within the range of 4500–250 cm-1 at 4 cm-1 intervals of spectral resolution, by averaging 40 scans. For the multivariate FTIR, spectral data were pre-processed using OriginPro 2021 software (OriginLab Corporation, Northampton, MA, USA). The measurements were performed at the Laboratory of the Department of Biophysics, University of Life Sciences in Lublin.

Atomic force microscopy (AFM)

The starch/NTA films were examined using AFM (MuliMode 8, Bruker Corporation, Santa Barbara, CA, USA) with PeakForce quantitative nanomechanics mapping (PFQNM)—tapping mode that combines topographical imaging with quantitative nanomechanical measurements. The mode employed a Vtespa 300 probe with a nominal spring constant of 42 N/m and a nominal tip radius of 5 nm (Bruker Corporation, Santa Barbara, CA, USA). The measurements were conducted under ambient conditions at 23 °C and with 50% RH. Each sample underwent scanning in three distinct, noncontinuous regions of 10 μm × 10 μm size, each measured at a digital resolution of 512 px × 512 px and scanning rate of 1 Hz. The resulting images were processed using Nanoscope Analysis (Bruker Corporation, Santa Barbara, CA, USA). The surface roughness Sa and root mean square (RMS) roughness Sq were obtained. Young's modulus was determined by fitting a linearized Derjaguin–

Muller–Toporov (DMT) model[69,70]. Additionally, the adhesion force, indicative of the interaction between the AFM probe and the sample surface, was determined.

Surface wettability

Contact angle measurements, employing the sessile drop method, were applied to evaluate the wettability of the starch/NTA film surfaces. An Attension Theta Lite optical goniometer (Biolin Scientific, Espoo, Finland) was used to determine the contact angle from the water droplet geometry. The measurements were performed under controlled conditions, at 23 °C and with 50% RH. A 6 µL deionized water drop was placed using a chromatography fixed-needle syringe, type 3, and Gauge 22s. For each new surface, the image was captured 3 s after deposition, and the measurement series consisted of 5 deposited drops. The readings from both sides of the drop were averaged and taken as the measured value.

Color measurement

The color of the starch/NTA films was determined using an X-Rite PANTONE spectrocolorimeter (X-Rite Inc., Grand Rapids, MI, USA) and expressed following the CIE L*a*b scale. Within the CIELAB color scale, the parameters of luminosity (L*: degree of lightness) and chromaticity (a*: red–green and b*: yellow–blue) were measured. A reference calibration plate with known L* = 96,678, a* = −0.699 and b* = 2.269 parameters was used to measure the background. The degree of color saturation C (Chroma) and the hue H (Hue) were additionally calculated based on the values of a* and b*.

Electronic absorption (UV-Vis) and fluorescence spectroscopies, resonance light scattering (RLS)

Electronic absorption spectra were recorded using a double-beam UV-vis Cary 300 Bio spectrophotometer (Varian) equipped with a thermostatted tray holder with a 6×6 multi-cell Peltier block. The temperature was controlled with a thermocouple probe (Cary Series II from Varian) placed directly in the sample.

Cary Eclipse spectrofluorometer (Varian) was employed for measurements of fluorescence excitation, emission, and synchronous spectra; all performed at 22 ^{0}C. The fluorescence spectra were recorded at 0.5 nm resolution after correcting for lamp and photomultiplier spectral characteristics.

RLS measurements were carried out according to the previously reported protocol 46 with synchronous scanning of both the excitation and emission monochromators (there was no interval between excitation and emission wavelengths) and a spectral resolution of 1.5 nm. Grams/AI 8.0 software (Thermo Electron Corporation; Waltham, Massachusetts, USA) was used to analyze the recorded data.

Fluorescence lifetimes – time-correlated single photon counting (TCSPC)

TCSPC measurements were performed using a FluoroCube fluorimeter (Horiba, France). The samples were excited with a pulsed NanoLED diode at 372 nm (pulse duration of 150 ps) operated with 1 MHz repetition. To avoid pulse pile-up, the power of the pulses was adjusted to an appropriate level using a neutral gradient filter. Fluorescence emission was recorded using a picosecond detector TBX-04 (IBH, JobinYvon, UK). DataStation and DAS6 software (JobinYvon, IBH, UK) was used for data acquisition and signal analysis. All fluorescence decays were measured in a 10 mm × 10 mm quartz cuvette, using an emitter cut-off filter with transmittance for wavelengths longer than 408 nm. The excitation profiles required for the deconvolution analysis were measured without the emitter filters using a light scattering cuvette. All measurements were performed in isopropanol at the temperature of 22 °C for selected concentrations. The properties of the starch/NTA film was also measured in an analogous setup. Each fluorescence decay was analyzed with a multiexponential model expressed by the equation:

$$I_t = \sum {}_i\alpha \, {}_i exp\left(-\frac{t}{\tau \, {}_i}\right)$$

where α_i and τ_i are the pre-exponential factor and the decay time of i-th component, respectively. Best-fit parameters were obtained through minimization of the reduced χ^2 value and residual distribution of the experimental data. The fractional contribution f_i of each decay time and the average lifetime of fluorescence decay ⟨τ⟩ were calculated based on the following equations:

$$f_i = \frac{\alpha \, {}_i\tau \, {}_i}{\sum {}_j\alpha \, {}_j\tau \, {}_j}$$

$$\langle\tau\rangle = \sum {}_i f_i\tau \, {}_i$$

Anisotropy Measurements

Steady-state fluorescence anisotropy (r) was calculated from the polarized components of fluorescence emission from the following formula:

$$r = \frac{I_{VV} - GI_{VH}}{I_{VV} + 2GI_{VH}}$$

where IVH is the intensity of the vertically excited, horizontally observed emission; IVV is the intensity of the vertically excited, vertically observed emission; and G is the geometrical factor correcting the system's polarization bias. A wire grid polarizer was used for the excitation to allow UV light transmission.

Computational details

Calculations were performed for both the monomeric and aggregated models of NTA using the Gaussian 16 package, version C.01[71]47, without explicitly imposing symmetry. All visualizations were made using either the GaussView 5.0.9[72]48 or the Mercury program. Starting geometries of monomer, dimer, and trimer forms of NTA were extracted from the X-ray crystal structure of the compound, compare with Figure S2.1.

Density functional theory (DFT) geometry optimizations were carried out with the global hybrid B3LYP[73–75]exchange-correlation functional and split-valence double-zeta basis set with one set of polarization and diffuse functions for all atoms, 6-31 + + G(d, p)[76777879808182]. Dispersion effects were accounted for in these calculations employing the third-generation Grimme's set of semiempirical dispersion corrections with the Becke-Johnson damping, D3[83,84]. Solvent (2-propanol, ε = 19.2640) effects were simulated using the polarizable continuum model (PCM)[85–87], with default parameters of the Gaussian/PCM implementation. All the obtained structures were subjected to frequencies calculations at the same level of theory in order to confirm that they represent energy minima (no imaginary frequencies) and also to evaluate free energy values.

Absorption (via calculations of vertical excitations from the ground state to the 50 lowest singlet excited states) and emission (via S_1excited-state geometry optimizations) properties were computed using time-dependent variant of DFT (TDDFT) with the dispersion-corrected range-separated hybrid ωB97X-D[88]density functional, split-valence triple-zeta basis set with one set of polarization and diffuse functions for all atoms, 6-311 + + G(d, p)[74,76,80,89,90]. The influence of the solvent (propan-2-ol) on excited-states features was modelled via linear response PCM[91,92].

To shed some light on the interaction mechanism between NTA and starch, additional geometry optimizations at the B3LYP + D3/6–31 + + G(d, p)/PCM(water, ε = 78.3553) level of theory were performed for simplified models of an NTA/starch complex with starch represented by either its α-D-glucose building unit or a truncated amylopectin molecule (see Figure S2.7). These were proceeded by a conformational search carried out with the semiempirical tight-binding based quantum chemistry method GFN2-xTB[93]and the generalized Born and surface area solvation (water) model (GBSA)[94]using iterative meta-dynamics with genetic structure crossing (iMTD-GC) approach[95]implemented in the conformer-rotamer ensemble sampling tool (CREST)[96].

Data availability

Data availability: The datasets used and/or analysed during the current study available from the corresponding author on reasonable request.

Received: 23 September 2024; Accepted: 9 December 2024
Published online: 28 December 2024

References

1. Joyce, K., Fabra, G. T., Bozkurt, Y. & Pandit, A. Bioactive potential of natural biomaterials: identification, retention and assessment of biological properties. *Signal. Transduct. Target. Therapy*. **6**, 1–28 (2021).
2. Lan, L., Ping, J., Xiong, J. & Ying, Y. Sustainable Natural Bio-Origin Materials for Future Flexible Devices. *Adv. Sci.* **9** (2022).
3. Ajmal, S., Athar Hashmi, F. & Imran, I. Recent progress in development and applications of biomaterials. *Materials Today: Proceedings* 62, 385–391 (2022).
4. Baranwal, J., Barse, B., Fais, A., Delogu, G. L. & Kumar, A. Biopolymer: A Sustainable Material for Food and Medical Applications. *Polymers* **14**, 983 (2022).
5. Janik, W., Jakubski, L., Kudła, S. & Dudek, G. Modified polysaccharides for food packaging applications: A review. *Int. J. Biol. Macromol.* **258**, (2024).
6. Hassan, F., Mu, B. & Yang, Y. Natural polysaccharides and proteins-based films for potential food packaging and mulch applications: A review. *Int. J. Biol. Macromol.* **70**, (2024).
7. Diaz-Baca, J. A. & Fatehi, P. Production and characterization of starch-lignin based materials: A review. *Biotechnol. Adv.* **70**, (2024).
8. Song, R. et al. Current development of biodegradable polymeric materials for biomedical applications. *Drug. Des. Devel. Ther.* **12**, 3117–3145 (2018).
9. Palanisamy, C. P., Cui, B., Zhang, H., Jayaraman, S. & Muthukaliannan, G. K. A comprehensive review on corn starch-based nanomaterials: Properties, simulations, and applications. *Polymers* **12**, 2161 (2020).
10. Jamróz, E., Kulawik, P. & Kopel, P. The effect of nanofillers on the functional properties of biopolymer-based films: A review. *Polymers* **11**, 675 (2019).
11. Tan, S. X. et al. A Comprehensive Review on the Emerging Roles of Nanofillers and Plasticizers towards Sustainable Starch-Based Bioplastic Fabrication. *Polymers* **14**, 664 (2022).
12. González-Arancibia, F. et al. Biopolymers as Sustainable and Active Packaging Materials: Fundamentals and Mechanisms of Antifungal Activities. *Biomolecules* 14, (2024).
13. Moeini, A., Germann, N., Malinconico, M. & Santagata, G. Formulation of secondary compounds as additives of biopolymer-based food packaging: A review. *Trends Food Sci. Technol.* **114**, 342–354 (2021).
14. Sharma, A., Prakash, P., Rawat, K., Solanki, P. R. & Bohidar, H. B. Antibacterial and Antifungal Activity of Biopolymers Modified with Ionic Liquid and Laponite. *Appl. Biochem. Biotechnol.* **177**, 267–277 (2015).
15. Hu, Y., Li, C. Y., Wang, X. M., Yang, Y. H. & Zhu, H. L. 1,3,4-Thiadiazole: Synthesis, reactions, and applications in medicinal, agricultural, and materials chemistry. *Chem. Rev.* **114**, 5572–5610 (2014).
16. Bala, M., Piplani, P., Ankalgi, A., Jain, A. & Chandel, L. 1,3,4-Thiadiazole: A Versatile Pharmacophore of Medicinal Significance. *Med. Chem.* **19**, 730–756 (2023).
17. Ahmad, S. et al. A review on recent progress in synthesis and biological activities of thiadiazole and its derivatives. *J. Mol. Struct.* **1312**, 138438 (2024).
18. Liu, F. & Chen, L. Thiadiazoles as potent inhibitors against corrosion of metals and alloys: Challenges and future prospects. *J. Mol. Liq.* **390**, 122904 (2023).
19. Wu, D. et al. Fluorescent chemosensors: The past, present and future. *Chem. Soc. Rev.* **46**, 7105–7123 (2017).
20. Rani, B. K. & John, S. A. Fluorogenic mercury ion sensor based on pyrene-amino mercapto thiadiazole unit. *J. Hazard. Mater.* **343**, 98–106 (2018).

21. Manna, A. K., Chowdhury, S. & Patra, G. K. Combined experimental and theoretical studies on a phenyl thiadiazole-based novel turn-on fluorescent colorimetric Schiff base chemosensor for the selective and sensitive detection of Al3+. *New J. Chem.* **44**, 10819–10832 (2020).
22. Zhao, J. et al. A 1,3,4-thiadiazole functionalized Schiff base based fluorescence enhancement and colorimetric probe for detection of Cu (II) ion and its potential applications. *Chem. Phys.* **565**, 111740 (2023).
23. Zong, H. et al. Physical mechanism of photoinduced intermolecular charge transfer enhanced by fluorescence resonance energy transfer. *Phys. Chem. Chem. Phys.* **20**, 13558–13565 (2018).
24. Sasaki, S., Drummen, G. P. C. & Konishi, G. I. Recent advances in twisted intramolecular charge transfer (TICT) fluorescence and related phenomena in materials chemistry. *J. Mater. Chem. C.* **4**, 2731–2743 (2016).
25. Wang, C. et al. Twisted intramolecular charge transfer (TICT) and twists beyond TICT: From mechanisms to rational designs of bright and sensitive fluorophores. *Chem. Soc. Rev.* **50**, 12656–12678 (2021).
26. Peng, X. et al. Synthesis and self-assembly of photoresponsive and luminescent polycatenar liquid crystals incorporating an azobenzene unit interconnecting two 1,3,4-thiadiazoles. *New J. Chem.* **41**, 2004–2012 (2017).
27. Kato, S. I. et al. A series of π-extended thiadiazoles fused with electron-donating heteroaromatic moieties: Synthesis, properties, and polymorphic crystals. *Chem.---Eur. J.* **21**, 3115–3128 (2015).
28. Gaber, M. & Al-Shihry, S. S. Spectrophotometric and electrical studies of charge transfer complexes of 2-amino-1,3,4-thiadiazole with π-acceptors. *Spectrochimica Acta - Part. A: Mol. Biomol. Spectrosc.* **62**, 526–531 (2005).
29. Budziak-Wieczorek, I. et al. Cooperativity of ESPT and Aggregation-Induced Emission Effects—An Experimental and Theoretical Analysis of a 1,3,4-Thiadiazole Derivative. *Int. J. Mol. Sci.* **25**, (2024).
30. Joshi, H. C. & Antonov, L. Excited-state intramolecular proton transfer: A short introductory review. *Molecules* **26**, 1475 (2021).
31. Samanta, P. K. & Misra, R. Intramolecular charge transfer for optical applications. *J. Appl. Phys.* **133**, (2023).
32. Czernel, G. et al. ESIPT-Related Origin of Dual Fluorescence in the Selected Model 1,3,4-Thiadiazole Derivatives. *Molecules* **25**, 4168 (2020).
33. Liao, C. T. et al. New metallomesogens derived from unsymmetric 1,3,4-thiodiazoles: synthesis, single crystal structure, mesomorphism, and optical properties. *Tetrahedron* **63**, 12437–12445 (2007).
34. Ila, Dani, R., Verma, S. P. & Krishnamoorthy, G. The origin of the longer wavelength emission in 2-(4-fluorophenylamino)-5-(2,4-dihydroxybenzeno)-1,3,4-thiadiazole and its analogue 2-phenylamino-5-(2-hydroxybenzono)-1,3,4-thiadiazole. *Photochemical Photobiological Sci.* **19**, 844–853 (2020).
35. Gu, J., Li, Z. & Li, Q. From single molecule to molecular aggregation science. *Coord. Chem. Rev.* **475**, 214872 (2023).
36. Mei, J., Leung, N. L. C., Kwok, R. T. K., Lam, J. W. Y. & Tang, B. Z. Aggregation-Induced Emission: Together We Shine, United We Soar! *Chem. Rev.* **115**, 11718–11940 (2015).
37. Liu, S. et al. Highly emissive D-A-π-D type aggregation-induced emission (AIE) or aggregation-induced emission enhancement (AIEE)-active benzothiadiazole derivatives with contrasting mechanofluorochromic features. *Spectrochimica Acta - Part. A: Mol. Biomol. Spectrosc.* **274**, 121122 (2022).
38. Wang, H. et al. Experimental and theoretical study on molecular aggregation and its effect on the photo-physical properties of the mesogenic bi-1,3,4-thiadiazole derivative. *Phys. Chem. Chem. Phys.* **13**, 9697–9705 (2011).
39. Matwijczuk, A. et al. Spectroscopic and Theoretical Studies of Fluorescence Effects in 2-Methylamino-5-(2,4-dihydroxyphenyl)-1,3,4-thiadiazole Induced by Molecular Aggregation. *J. Fluoresc.* **28**, 65–77 (2018).
40. Budziak, I. et al. Spectroscopic and theoretical investigation into substituent- and aggregation-related dual fluorescence effects in the selected 2-amino-1,3,4-thiadiazoles. *J. Mol. Liq.* **291**, 111261 (2019).
41. Kukhta, N. A. & Bryce, M. R. Dual emission in purely organic materials for optoelectronic applications. *Mater. Horiz.* **8**, 33–55 (2021).
42. Behera, S. K., Park, S. Y. & Gierschner, J. Dual Emission: Classes, Mechanisms, and Conditions. *Angewandte Chemie - Int. Ed.* **60**, 22624–22638 (2021).
43. Wang, H. et al. Breaching Kasha's rule for dual emission: Mechanisms, materials and applications. *J. Mater. Chem. C.* **9**, 10154–10172 (2021).
44. Budziak-Wieczorek, I. et al. Spectroscopic characterization and assessment of microbiological potential of 1,3,4-thiadiazole derivative showing ESIPT dual fluorescence enhanced by aggregation effects. *Sci. Rep.* **12**, 22140 (2022).
45. Cornellas, A. et al. Self-aggregation and antimicrobial activity of imidazolium and pyridinium based ionic liquids in aqueous solution. *J. Colloid Interface Sci.* **355**, 164–171 (2011).
46. Moore, S. A., Frazier, S. M., Sibbald, M. S., Degraff, B. A. & Demas, J. N. On the causes of altered photophysics of luminescent metal complexes embedded in polymer hosts. *Langmuir* **27**, 9567–9575 (2011).
47. Lyu, G. et al. Aggregation-induced emission from silole-based lumophores embedded in organic-inorganic hybrid hosts. *J. Mater. Chem. C.* **9**, 13914–13925 (2021).
48. Machida, T., Taniguchi, R., Oura, T., Sada, K. & Kokado, K. Liquefaction-induced emission enhancement of tetraphenylethene derivatives. *Chem. Commun.* **53**, 2378–2381 (2017).
49. Volkova, T. V., Domanina, E. N., Chislov, M. V., Proshin, A. N. & Terekhova, I. V. Polymeric composites of 1,2,4-thiadiazole: solubility, dissolution and permeability assay. *J. Therm. Anal. Calorim.* **140**, 2305–2315 (2020).
50. Combrzyński, M. et al. Selected Physical and Spectroscopic Properties of TPS Moldings Enriched with Durum Wheat Bran. *Materials* **15**, 5061 (2022).
51. Li, C. et al. Highly Productive Synthesis, Characterization, and Fluorescence and Heavy Metal Ion Adsorption Properties of Poly(2,5-dimercapto-1,3,4-thiadiazole) Nanosheets. *Polymers* 10, 24 (2017).
52. Riyadh, S. M., Khalil, K. D. & Aljuhani, A. Chitosan-MgO Nanocomposite: One Pot Preparation and Its Utility as an Ecofriendly Biocatalyst in the Synthesis of Thiazoles and [1,3,4]thiadiazoles. *Nanomaterials* **8**, 928 (2018).
53. Alshaye, N. A., Riyadh, S. M., Khalil, K. D., Alharbi, N. S. & Ahmed, H. A. Eco-synthesis route: Developing bis-hydrazono[1,2,4]-thiadiazoles via a green synthetic approach with calcium oxide-chitosan nanocomposite. *Int. J. Biol. Macromol.* **273**, 132815 (2024).
54. Kim, S. Y. et al. Excitation spectroscopic and synchronous fluorescence spectroscopic analysis of the origin of aggregation-induced emission in: N, N -diphenyl-1-naphthylamine- o -carborane derivatives. *Phys. Chem. Chem. Phys.* **20**, 17458–17463 (2018).
55. Arsov, Z., Urbančič, I. & Štrancar, J. Aggregation-induced emission spectral shift as a measure of local concentration of a pH-activatable rhodamine-based smart probe. *Spectrochimica Acta - Part. A: Mol. Biomol. Spectrosc.* **190**, 486–493 (2018).
56. Schleyer, K. A. et al. Responsive Fluorophore Aggregation Provides Spectral Contrast for Fluorescence Lifetime Imaging. *ChemBioChem* **21**, 2196–2204 (2020).
57. Pasternack, R. F. & Collings, P. J. Resonance light scattering: A new technique for studying chromophore aggregation. *Science* **269**, 935–939 (1995).
58. Pasternack, R. F., Giannetto, A., Bustamante, C., Collings, P. J. & Gibbs, E. J. Porphyrin Assemblies on DNA as Studied by a Resonance Light-Scattering Technique. *J. Am. Chem. Soc.* **115**, 5393–5399 (1993).
59. Parkash, J. et al. Depolarized resonance light scattering by porphyrin and chlorophyll a aggregates. *Biophys. J.* **74**, 2089–2099 (1998).
60. Kasha, M. Energy Transfer Mechanism and the Molecular Exciton Model for Molecular Aggregates. *Radiat. Res.* **20**, 55–70 (1963).
61. Spano, F. C. & Silva, C. H. J-aggregate behavior in polymeric semiconductors. *Annu. Rev. Phys. Chem.* **65**, 477–500 (2014).
62. Brixner, T., Hildner, R., Köhler, J., Lambert, C. & Würthner, F. Exciton Transport in Molecular Aggregates – From Natural Antennas to Synthetic Chromophore Systems. *Adv. Energy Mater.* **7**, 1700236 (2017).

63. Hestand, N. J. & Spano, F. C. Expanded Theory of H- and J-Molecular Aggregates: The Effects of Vibronic Coupling and Intermolecular Charge Transfer. *Chem. Rev.* **118**, 7069–7163 (2018).
64. Eder, T. et al. Interplay Between J- and H-Type Coupling in Aggregates of π-Conjugated Polymers: A Single-Molecule Perspective. *Angew. Chem. Int. Ed.* **58**, 18898–18902 (2019).
65. Ma, S. et al. Organic molecular aggregates: From aggregation structure to emission property. *Aggregate* **2**, e96 (2021).
66. Panthakkal Das, P., Mazumder, A., Rajeevan, M., Swathi, R. S. & Hariharan, M. Energy landscape of perylenediimide chromophoric aggregates. *Phys. Chem. Chem. Phys.* **26**, 2007–2015 (2023).
67. Broeren, M. L. M., Kuling, L., Worrell, E. & Shen, L. Environmental impact assessment of six starch plastics focusing on wastewater-derived starch and additives. *Resour. Conserv. Recycl.* **127**, 246–255 (2017).
68. Yadav, K. & Nikalje, G. C. Comprehensive analysis of bioplastics: life cycle assessment, waste management, biodiversity impact, and sustainable mitigation strategies. *PeerJ* **12**, 1–29 (2024).
69. Kwaśniewska, A., Świetlicki, M., Prószyński, A. & Gładyszewski, G. The quantitative nanomechanical mapping of starch/kaolin film surfaces by Peak Force AFM. *Polymers* **13**, 1–11 (2021).
70. Derjaguin, B. V., Muller, V. M. & Toporov, Y. P. Effect of contact deformations on the adhesion of particles. *J. Colloid Interface Sci.* **53**, 314–326 (1975).
71. Frisch, M. J. et al. *Gaussian 16, Revision C01. Gaussian 16, Revision C.01* (Gaussian, Inc., 2016).
72. Dennington, R. & Keith, T. A. & J. M. Millam. GaussView, Version 5.0.9. (2009).
73. Becke, A. D. Density-functional thermochemistry. III. The role of exact exchange. *J. Chem. Phys.* **98**, 5648–5652 (1993).
74. Lee, C., Yang, W. & Parr, R. G. Development of the Colle-Salvetti correlation-energy formula into a functional of the electron density. *Phys. Rev. B.* **37**, 785–789 (1988).
75. Stephens, P. J., Devlin, F. J., Chabalowski, C. F. & Frisch, M. J. Ab Initio calculation of vibrational absorption and circular dichroism spectra using density functional force fields. *J. Phys. Chemistry*.* **98**, 11623–11627 (1994).
76. Clark, T., Chandrasekhar, J., Spitznagel, G. W. & Schleyer, P. V. R. Efficient diffuse function-augmented basis sets for anion calculations. III. The 3-21 + G basis set for first-row elements, Li–F. *J. Comput. Chem.* **4**, 294–301 (1983).
77. Ditchfield, R., Hehre, W. J. & Pople, J. A. Self-consistent molecular-orbital methods. IX. An extended gaussian-type basis for molecular-orbital studies of organic molecules. *J. Chem. Phys.* **54**, 720–723 (1971).
78. Francl, M. M. et al. Self-consistent molecular orbital methods. XXIII. A polarization-type basis set for second-row elements. *J. Chem. Phys.* **77**, 3654–3665 (1982).
79. Gordon, M. S., Binkley, J. S., Pople, J. A., Pietro, W. J. & Hehre, W. J. Self-Consistent Molecular-Orbital Methods. 22. Small Split-Valence Basis Sets for Second-Row Elements. *J. Am. Chem. Soc.* **104**, 2797–2803 (1982).
80. Hariharan, P. C. & Pople, J. A. The influence of polarization functions on molecular orbital hydrogenation energies. *Theoret. Chim. Acta*. **28**, 213–222 (1973).
81. Hehre, W. J., Ditchfield, K. & Pople, J. A. Self-consistent molecular orbital methods. XII. Further extensions of gaussian-type basis sets for use in molecular orbital studies of organic molecules. *J. Chem. Phys.* **56**, 2257–2261 (1972).
82. Spitznagel, G. W., Clark, T., von Ragué Schleyer, P. & Hehre, W. J. An evaluation of the performance of diffuse function-augmented basis sets for second row elements, Na-Cl. *J. Comput. Chem.* **8**, 1109–1116 (1987).
83. Grimme, S., Antony, J., Ehrlich, S. & Krieg, H. A consistent and accurate ab initio parametrization of density functional dispersion correction (DFT-D) for the 94 elements H-Pu. *J. Chem. Phys.* **132**, (2010).
84. Grimme, S., Ehrlich, S. & Goerigk, L. Effect of the damping function in dispersion corrected density functional theory. *J. Comput. Chem.* **32**, 1456–1465 (2011).
85. Tomasi, J., Mennucci, B. & Cammi, R. Quantum mechanical continuum solvation models. *Chem. Rev.* **105**, 2999–3093 (2005).
86. Cossi, M., Barone, V., Cammi, R. & Tomasi, J. Ab initio study of solvated molecules: A new implementation of the polarizable continuum model. *Chem. Phys. Lett.* **255**, 327–335 (1996).
87. Scalmani, G. & Frisch, M. J. Continuous surface charge polarizable continuum models of solvation. I. General formalism. *J. Chem. Phys.* **132**, (2010).
88. Chai, J. D. & Head-Gordon, M. Long-range corrected hybrid density functionals with damped atom-atom dispersion corrections. *Phys. Chem. Chem. Phys.* **10**, 6615–6620 (2008).
89. Krishnan, R., Binkley, J. S., Seeger, R. & Pople, J. A. Self-consistent molecular orbital methods. XX. A basis set for correlated wave functions. *J. Chem. Phys.* **72**, 650–654 (1980).
90. McLean, A. D. & Chandler, G. S. Contracted Gaussian basis sets for molecular calculations. I. Second row atoms, Z = 11–18. *J. Chem. Phys.* **72**, 5639–5648 (1980).
91. Cossi, M. & Barone, V. Time-dependent density functional theory for molecules in liquid solutions. *J. Chem. Phys.* **115**, 4708–4717 (2001).
92. Scalmani, G. et al. Geometries and properties of excited states in the gas phase and in solution: Theory and application of a time-dependent density functional theory polarizable continuum model. *J. Chem. Phys.* **124**, 94107 (2006).
93. Bannwarth, C., Ehlert, S. & Grimme, S. GFN2-xTB - An Accurate and Broadly Parametrized Self-Consistent Tight-Binding Quantum Chemical Method with Multipole Electrostatics and Density-Dependent Dispersion Contributions. *J. Chem. Theory Comput.* **15**, 1652–1671 (2019).
94. Brieg, M., Setzler, J., Albert, S. & Wenzel, W. Generalized Born implicit solvent models for small molecule hydration free energies. *Phys. Chem. Chem. Phys.* **19**, 1677–1685 (2017).
95. Grimme, S. Exploration of Chemical Compound, Conformer, and Reaction Space with Meta-Dynamics Simulations Based on Tight-Binding Quantum Chemical Calculations. *J. Chem. Theory Comput.* **15**, 2847–2862 (2019).
96. Pracht, P., Bohle, F. & Grimme, S. Automated exploration of the low-energy chemical space with fast quantum chemical methods. *Phys. Chem. Chem. Phys.* **22**, 7169–7192 (2020).

Acknowledgements

This research has been made possible by the Kosciuszko Foundation—the American Center of Polish Culture. We gratefully acknowledge the Polish high-performance computing infrastructure PLGrid (HPC Centers: ACK Cyfronet AGH, WCSS) for providing computer facilities and support within computational grant no. PLG/2023/016770.

Author contributions

A.K. and G.G. wrote the part of the manuscript related to AFM measurements and other physicochemical studies. They prepared the figures for this section of the work. They also prepared the sample for spectroscopic measurements.K.O. and M.S-H. performed quantum mechanical DFT calculations and wrote that section of the manuscript. They also prepared the figures for this part.M.S-H. wrote the main part of the manuscript together with A.M. and supervised the main part of the manuscript alongside A.M. She also discussed the theoretical aspects of the work with A.M. and assisted in the discussion of the spectroscopic part.D.K. synthesized the compound and described this part of the research. He prepared the figures for this section of the work.K.Rz.,

L.C., and B.G. performed absorption, fluorescence emission, excitation spectra, and RLS measurements, processed the results, and prepared the figures from this section for publication.M.F. measured the fluorescence lifetimes and described this part of the work.A.A.H. and M.N. carried out the crystallization of the compound and described the results of this part of the work. They also prepared the figures for this section.A.M. wrote the main part of the manuscript, conceived the idea for the article, assisted with and supervised the spectroscopic measurements, and was the originator of the main theme of the work. A.M. also supervised the entire project. The manuscript was written through contributions of all authors. All authors have given approval to the final version of the manuscript.

Declarations

Competing interests

The authors declare no competing interests.

Additional information

Supplementary Information The online version contains supplementary material available at https://doi.org/10.1038/s41598-024-82853-2.

Correspondence and requests for materials should be addressed to M.S.-H. or A.M.

Reprints and permissions information is available at www.nature.com/reprints.

Publisher's note Springer Nature remains neutral with regard to jurisdictional claims in published maps and institutional affiliations.